

# Design and characterisation of the Pointing LEDs for the Medium-Sized Telescopes of CTA

Bachelor's Thesis in Physics

Presented by  
**Christina Matzke**  
30.09.2024

Erlangen Centre for Astroparticle Physics  
Friedrich-Alexander-Universität Erlangen-Nürnberg

Supervisor: Prof. Dr. Christopher van Eldik



## Abstract

The Cherenkov Telescope Array Observatory (CTAO) will host telescopes in three different sizes for detection and direction reconstruction of Cherenkov light generated by gamma radiation up to very high energies. A precise pointing method is essential to fulfil the requirements on the pointing accuracy of these telescopes.

The pointing method of the Medium-Sized Telescopes of CTAO is based on twelve LEDs mounted around the centre of the Cherenkov camera in circular shape. The pointing camera images the sky and the LEDs simultaneously, and a ring fit is performed to determine the Cherenkov camera centre. Hence, a position correlation between the telescope and the night sky is obtained.

In the scope of this thesis a mock-up of the Cherenkov camera front with twelve LEDs on predefined positions is constructed and imaged by the pointing camera in two series. An adjustment of intensity and spot width is done by a current control, a combination of filter and diffuser and a modification of the pinhole size in order to adapt the spot shapes and peak values to those of the stars.

The image series are evaluated concerning the LED positions and the deviation of those. The resulting LED localisation precision is  $\sigma \lesssim 0.05$  arcsec and therefore contributes to the pointing accuracy criterion of 7 arcsec by less than 1 % only. Hence, the described LED monitoring method delivers sufficiently precise position determination, considering deviations within the limits which are given by the Cherenkov Telescope Array Observatory.





## Zusammenfassung

Das Cherenkov Telescope Array Observatory (CTAO) wird Gammastrahlung bis in sehr hohe Energiebereiche hinein detektieren und deren Herkunftsrichtung rekonstruieren. Dafür sind Teleskope in drei verschiedenen Größen vorgesehen, die das durch Gammastrahlung erzeugte Cherenkovlicht messen. Um die Anforderungen an die Messgenauigkeit der Teleskopausrichtung zu erfüllen, ist eine präzise Ausrichtungsmethode („Pointingmethode“) erforderlich.

Die entwickelte Pointingmethode der mittelgroßen Teleskope (Medium-Sized Telescopes, MSTs) von CTAO basiert auf einer kreisförmigen Anordnung von zwölf LEDs um das Zentrum der Cherenkovkamera. Eine Pointingkamera bildet Sterne und LEDs zugleich ab, wodurch die Position des Teleskops in Korrelation zum Nachthimmel gebracht wird. Dazu wird das Zentrum der Cherenkovkamera anhand eines Kreisfits ermittelt.

Im Rahmen dieser Arbeit wird eine Nachbildung der Vorderseite der Cherenkovkamera erstellt, auf der die LEDs in ihren vordefinierten Positionen montiert sind. Mit der Pointingkamera werden davon Bilder in zwei Messreihen aufgenommen. Mithilfe des LED-Stroms und einer Kombination aus einem Filter und einem Diffusor sowie nachjustierte Pinholegröße werden Intensität und Spotbreite an die der Sterne angepasst.

Die Messreihen werden hinsichtlich der LED-Positionen und deren Abweichungen ausgewertet. Die daraus resultierende Präzision, mit der die LEDs lokalisiert werden können, ergibt sich zu  $\sigma \lesssim 0.05 \text{ arcsec}$ , und trägt folglich mit weniger als 1 % zum gesamten Fehlerbudget bei, das mit 7 arcsec als Pointingkriterium durch CTA festgelegt ist. Die beschriebene Methode zur LED-Abbildung liefert damit hinreichend präzise Positionswerte, deren Abweichungen sich im Rahmen der durch CTAO vorgegebenen Grenzen bewegen.



# Contents

<b>1</b>	<b>Gamma-ray astronomy and Cherenkov telescopes</b>	<b>2</b>
1.1	Astrophysical methods and aims of the Cherenkov Telescope Array . . .	2
1.2	Design of the Medium-Sized Telescope of the Cherenkov Telescope Array	4
<b>2</b>	<b>Pointing technique for the Medium-Sized Telescopes</b>	<b>6</b>
2.1	Pointing accuracy criterion . . . . .	6
2.2	The pointing correction concept . . . . .	6
2.3	The pointing camera . . . . .	7
2.4	Pointing software architecture . . . . .	8
<b>3</b>	<b>Preparatory measurements and considerations</b>	<b>11</b>
3.1	Thermal stability . . . . .	11
3.2	Focusing of the pointing camera . . . . .	11
3.3	Intensity adjustments . . . . .	11
3.3.1	LED current . . . . .	13
3.3.2	Intensity attenuation with filter and diffuser . . . . .	14
<b>4</b>	<b>Verification of the pointing criterion using a FlashCam mock-up</b>	<b>22</b>
4.1	The FlashCam mock-up . . . . .	22
4.2	Optimisation of the pinhole size . . . . .	23
4.3	Analysis of the set-up stability . . . . .	26
4.4	Time-dependent analysis of the LED positions . . . . .	32
4.4.1	Movement of LED positions . . . . .	32
4.4.2	Deviations of LED positions and pointing precision . . . . .	35
<b>5</b>	<b>Summary and Outlook</b>	<b>39</b>
<b>A</b>	<b>Appendix</b>	<b>45</b>
	<b>Bibliography</b>	<b>60</b>



# 1 Gamma-ray astronomy and Cherenkov telescopes

The impressive scientific potential of ground-based gamma-ray astronomy has resulted in the worldwide development and construction of several Imaging Air Cherenkov Telescopes (IACTs) in the last few decades. The current generation of instruments with up to five individual telescopes includes projects such as the High Energy Stereoscopic System (H.E.S.S.) in Namibia, Major Atmospheric Gamma-ray Imaging Cherenkov telescopes (MAGIC) in La Palma and Very Energetic Radiation Imaging Telescope Array System (VERITAS) in Arizona and has successfully detected about 200 gamma-ray emitting sources.

The Cherenkov Telescope Array (CTA) for very high energy gamma-ray astronomy is planned to be the next-generation observatory, covering an extended gamma-ray energy range from about 20 GeV to 300 TeV. Its improved performance is expected to expand the number of known objects in gamma-ray astronomy by up to a thousand new sources. It will set a new benchmark for our understanding of cosmic particles, extreme environments in the universe and exploring frontiers in physics concerning e.g. profound understanding of pulsar wind nebula, supernova remnants or the Galactic centre. The project contains telescope locations in the northern and southern hemisphere. The Spanish isles of La Palma host CTA North. For the Southern Hemisphere Array of the Cherenkov Telescope Array Observatory (CTAO) the isolated location of the Atacama Desert in Chile is chosen, protecting the telescopes from light pollution and offering both, adequate atmospheric conditions and large space for the required number of telescopes. The Northern and Southern Hemisphere Arrays will host more than 60 telescopes together. Therefore, CTA will be the largest collection of Cherenkov telescopes on the planet and will substantially increase the chance for discovery and deeper exploration of gamma-ray sources (CTA-website, 2024c; U. Schwanke et al., 2022).

Section 1 provides an introduction to atmospheric air showers, the production of Cherenkov radiation, and its detection by IACTs. Further, it will introduce the Medium-Sized Telescopes (MSTs) for the southern location of CTA.

## 1.1 Astrophysical methods and aims of the Cherenkov Telescope Array

The CTAO will study extreme environments which are home to the most energetic objects in the universe, like supermassive black holes and supernova remnants. These are investigated as candidates able to accelerate charged particles (mostly hadrons) to the observed energies by means of shock-front acceleration, relativistic jets and other mechanisms. The interaction of those particles with matter, magnetic fields, or light in the vicinity of their source or in interstellar space generates secondary gamma radiation via synchrotron radiation, inverse Compton scattering or  $\pi^0$ -decay (CTA-website, 2024e; Lahmann, 2022).

On the way from the cosmic source to the earth, the hadronic particles need to traverse the interstellar medium (ISM) which hosts magnetic fields, deflecting them. Gamma radiation comes along with a great advantage: on the way from its cosmic source to earth it travels mostly undeflected. Therefore, its entry direction to the atmosphere

directly points back to its source. Interacting with the atmosphere, gamma-rays initiate electromagnetic air showers which start with pair production of the incident photon. The generated electron-positron pair is subject to bremsstrahlung, generating new photons with lower energies. These two effects continue in form of a cascade. The particles resulting from this processes can travel faster than light in the medium (the Earth's atmosphere) which leads to the characteristic blue Cherenkov light. The Cherenkov flashes occur in a timescale of nanoseconds and have a cone shape. Its opening angle is determined by both, the velocity of the particle and the refraction index of the medium.

The emitted Cherenkov light can be measured by IACTs. These telescopes allow a reconstruction of the energy of the incident photon and in case of two or more instruments being used, of its direction (CTA-website, 2024f; Lahmann, 2022).

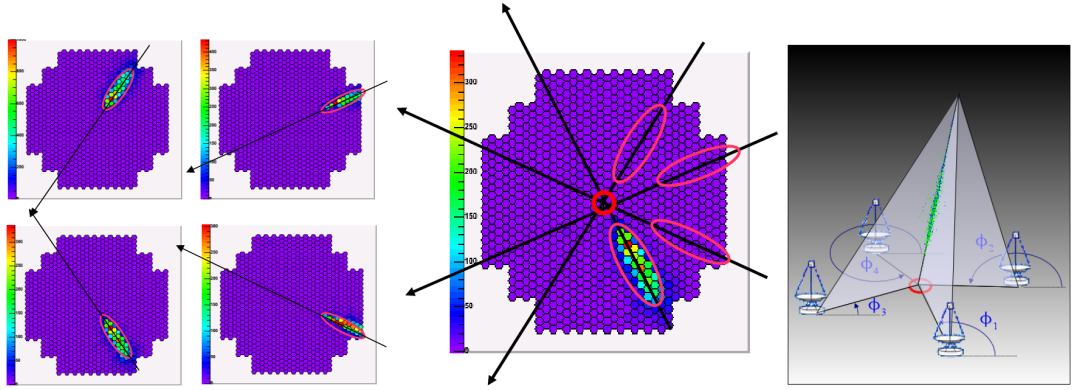


Figure 1: Illustration of the stereoscopic Cherenkov technique using four telescopes. Reconstruction of the shower impact point on the ground (left), in the sky (centre), and the shower reconstruction in 3D (right). Taken from Naurois (2015).

The illustration in Figure 1 shows the reconstruction of the shower direction. The electromagnetic shower has an elliptical shape on the single telescopes (left image). The projected shower axis corresponds to the elliptical major axis. From the projection of the four IACTs to one image the intersection point of the major axes can be derived (image in the middle). From this intersection point the direction of the shower can be reconstructed (right image).

In case of a wrong reconstruction for one telescope (e.g. misalignment of the camera), the intersection point of the major axes will shift. The more telescopes are imaging the shower, the lower is the impact of one telescope on the reconstruction. In the scenario of an unforeseen systematic misalignment of all participating telescopes, e.g. mast bending, wind load, etc., the intersection point will shift from its original position. Consequently, precise pointing is strongly required for all IACTs to achieve a reliable shower reconstruction.

CTAO requires three classes of telescopes (small-, medium- and large-sized) to cover the planned energy range. The alpha layout of CTA South has 14 Medium-Sized Telescopes (MSTs) to support direction reconstruction with an accuracy of 7 arcsec.

Based on the physical geometry of the MST (introduced in the following section) this angular requirement can be translated into a  $\approx 0.6$  mm spacial shift on the camera's focal plane. (Garczarczyk, 2022b).

## 1.2 Design of the Medium-Sized Telescope of the Cherenkov Telescope Array

The alpha layout of CTA South consists of 37 Small-Sized Telescopes (SSTs) to detect the highest energy spectrum of gamma-rays and 14 Medium-Sized Telescopes (MSTs) to deal with the core energy range of 150 GeV to 5 TeV. The construction of four Large-Sized Telescopes (LSTs) and three more SSTs is prepared to enable an enlargement of the array in the future (CTA-website, 2024a; CTA-website, 2024d).

The design of the MSTs, shown in Figure 2, follows the classical (but modified) Davies-Cotton design (a single spherical dish with several spherical mirrors), which has been used extensively in existing Cherenkov telescope projects (CTA Consortium, 2010; CTA-website, 2024b).

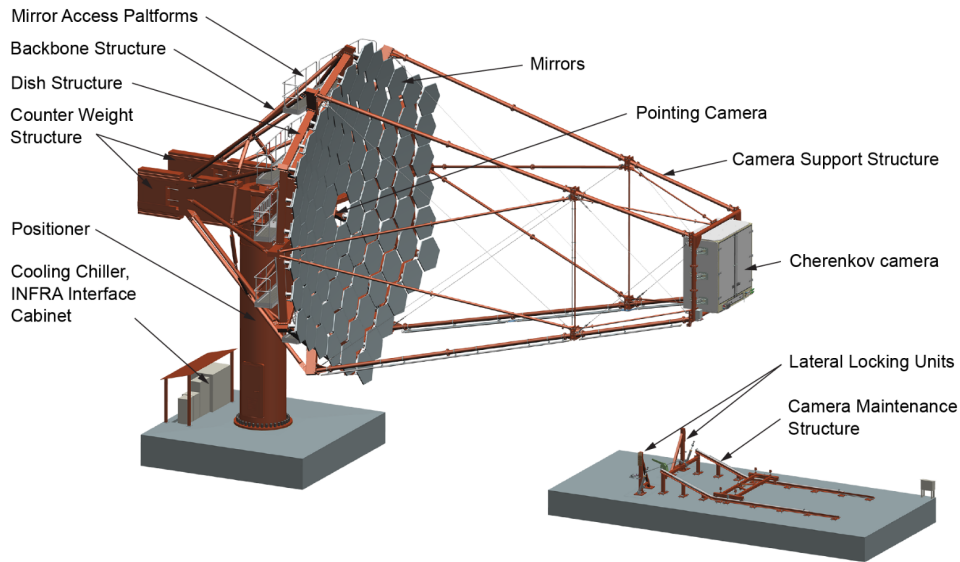


Figure 2: Design of the MST with its main assemblies, amongst the Cherenkov camera and the pointing camera. Taken from Garczarczyk (2022b).

The tessellated telescope mirror has a diameter of about 12 m and a curvature radius of about 19.2 m. Each of the 86 hexagonal-shaped spherical mirror facets is mounted on an active mirror control assembly. The full mirror assembly has an effective focal length<sup>1</sup> of 16 m. Incident Cherenkov light is collected by 88 m<sup>2</sup> reflector surface and focused onto the Cherenkov camera's focal plane (compare Figure 2).

For CTA North, the so-called NectarCam is used, whereas CTA South will use the so-called FlashCam (compare Figure 3) as the Cherenkov camera. The latter is relevant

<sup>1</sup>Commonly referred to as just the telescope's focal length

for this thesis and is now explained further. Both Cherenkov camera types are based on photomultiplier tubes (PMTs) as photo detection pixels. The FlashCam comprises 1764 pixels and a Flash Analog-to-Digital Converter (FADC) based data acquisition system in order to process and store the PMT signals. The Field-of-View (FoV) is  $\approx 8^\circ$ . (CTA-website, 2024b; U. Schwanke et al., 2022).

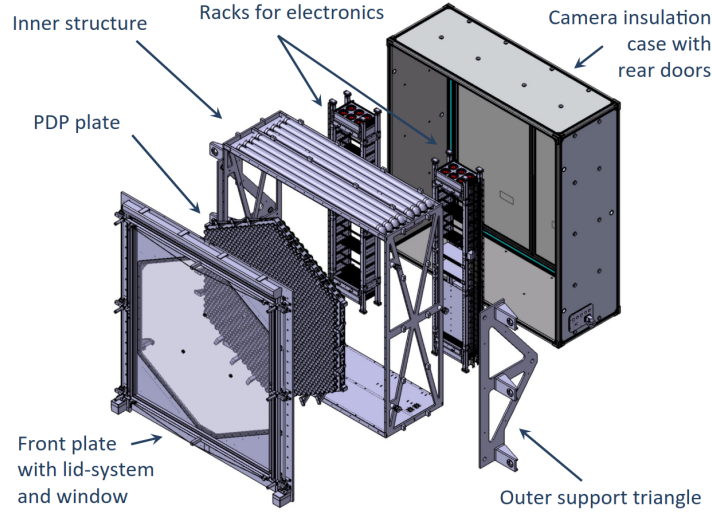


Figure 3: CAD explosion model of the FlashCam design. Taken from G. Pühlhofer (2015).

On its front plate twelve LEDs are installed on fixed positions in circular shape. Together with a Pointing Camera (PCAM) in the centre of the mirror dish, these LEDs serve as a basis for an accurate measurement of the pointing of the Southern MSTs. The next chapter introduces the properties of the optical pointing camera, elucidates the details of the pointing method and criterion and gives a short overview over the required software architecture.



## 2 Pointing technique for the Medium-Sized Telescopes

In order to guarantee an accurate pointing of the MST, the position of the Cherenkov camera with respect to the optical axis must be measured. Therefore, the optical pointing camera and the pointing concept are depicted, the pointing software is explained and an outline is given of how the pointing criterion of CTA will be verified in the following chapters.

### 2.1 Pointing accuracy criterion

The aim of this thesis is to decide whether the planned LED based pointing concept and set-up of the MSTs of CTA are precise enough to fulfil the CTA pointing accuracy requirement of 7 arcsec, which has not been verified yet.

For this thesis a mock-up of the FlashCam is built, copying its sizes and adopting the positions of the twelve pointing LEDs. Several preparation measurements have to be performed, e.g. the focus of PCAM or the right choice of neutral density (ND) filters for intensity attenuation of the LEDs. Then the set-up is constructed and adjusted, including the alignment of PCAM and the accurate positioning of the LEDs. PCAM measurements of the LED circle are analysed regarding several variables (amongst others flux, peak or camera temperature). The LED positions are determined by a centre-of-gravity reconstruction, then the centre of the LED circle is determined by a ring fit<sup>2</sup>. Finally, the precision of the circle centre determination reached with this method is discussed in terms of the pointing criterion.

### 2.2 The pointing correction concept

The outline in this chapter as well as in chapter 2.3 follows the technical report from Garczarczyk (2022b) and the paper from U. Schwanke et al. (2022). Local and instrumental conditions influence the pointing direction of the telescope, hence accurate calibration is necessary. PCAM measures the position of the Cherenkov camera and the stars with respect to the MST structure. For this purpose it is mounted in the centre of the mirror and aligned with the optical axis of the MST. Contrary to existing designs, this SingleCCD concept enables PCAM to image the pointing LEDs on the Cherenkov camera front plate and the stars simultaneously. The concept is shown in Figure 4. The pointing calibration is split in two procedures:

- **Dedicated pointing calibration runs**

Conclusions on the optical axis of the telescope can be drawn by targeting bright stars and imaging them on the focal plane of the Cherenkov camera. Simultaneously, the plane of the Cherenkov camera can be imaged by the LEDs. By recording both the reflected stars and the LEDs, PCAM enables the reconstruction of the intersection point of the telescope axis with the FlashCam plane. This allows corrections of misalignment and elastic deformations (like mast bending or dish deformation) by a pointing model.

---

<sup>2</sup>To be exact, parameters of a more complex coordinate transformation between camera pixel coordinates and coordinates on the camera plate are fitted including rotation and tilts. However, in this work we concentrate on the parameters of focal length and rotation.

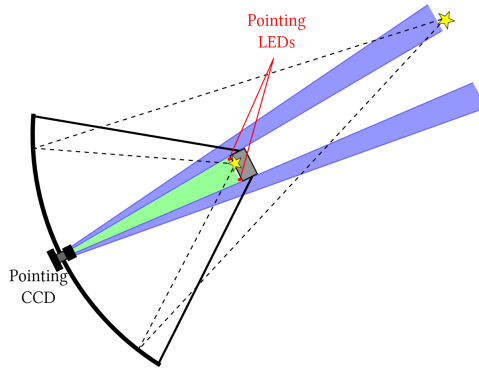


Figure 4: SingleCCD pointing concept. Taken from Herpich (2010).

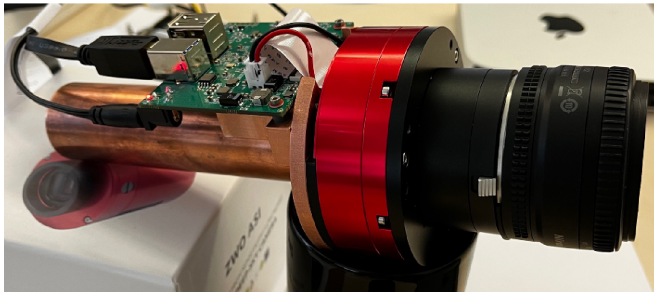
- **In-operation corrections**

The pointing model found in the previous step predicts star positions around the FlashCam so that the corresponding orientation of the FlashCam can be obtained. Its actual orientation can be deduced from the LEDs and both is compared in order to correct inelastic deformations like wind loads on the telescope construction.

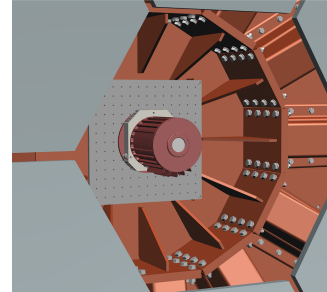
### 2.3 The pointing camera

The optical camera chosen for the pointing measurements is the ZWO ASI2600MM Pro (Figure 5) which consists of a CMOS sensor with a resolution of  $6248 \times 4176$  pixels and a pixel size of  $3.76 \mu\text{m}$  and supports an exposure time range of  $32 \mu\text{s}$  to 2000 s. The sensor can be cooled up to  $35^\circ\text{C}$  below ambient temperature (Zwoastro, 2021).

The ZWO ASI2600MM Pro was chosen due to several advantages: its peak quantum efficiency of 91 % and low noise. The active chip cooling reduces the dark current noise and prevents a temperature-dependent expansion of the chip which influences the pointing accuracy and hence is a substantial instrumental systematic uncertainty. The used lens (Nikon AF NIKKOR 50mm f/1.8) enables a Field-of-View (FoV) of  $26.5^\circ \times 17.8^\circ$  and a resolution of about 15'' per pixel on the sky. The lens is operated at an aperture of f/11.



(a) PCAM prototype set-up



(b) PCAM position

Figure 5: PCAM: (a) Internal components of PCAM prototype (ZWO ASI2600MM Pro) and (b) its proposed mounting position in the centre of the MST mirror dish. (b) is taken from Garczarczyk (2022b).

PCAM includes a computer (MIO-2361EW-S1A2 from Advantech) for hardware control and software communication purposes inside its custom-made aluminum casing. On its rear side PCAM is mounted on a thermally coupled copper support element. It is fixed rigidly to its casing by a support structure to avoid distortion or bending. The back heat sink of the camera is replaced by a copper tube to interface with the camera back side. Figure 6 also shows the positions of the power control PCB, the camera interface PCB and the Ethernet link. An anti-reflective glass window with a heating element protects the set-up from environmental impacts.

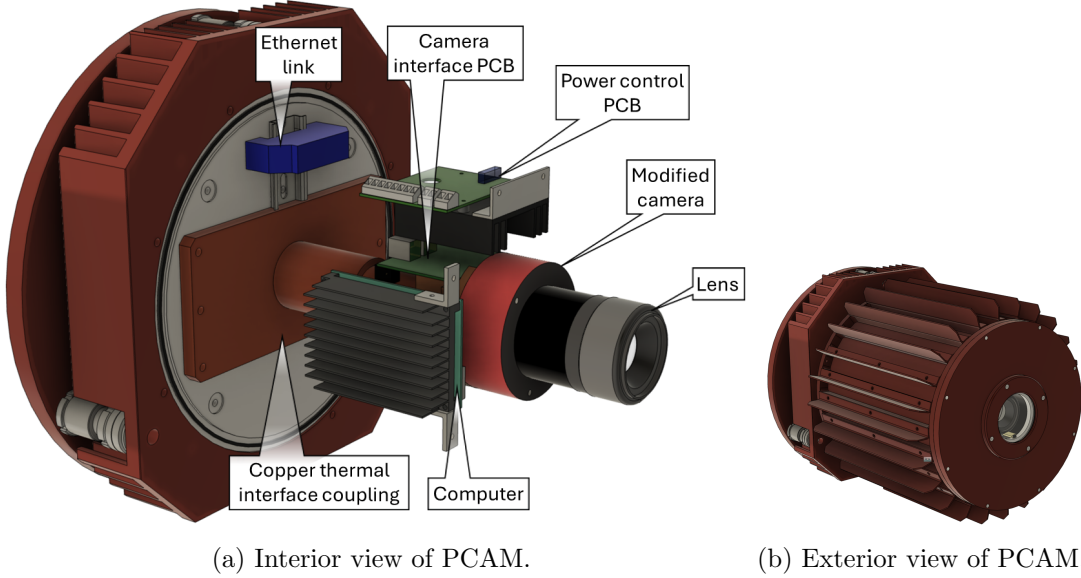


Figure 6: CAD 3D model of PCAM housing and the components inside.

In the centre of the dish PCAM is installed with a distance of 16 m to the front of the FlashCam. It is focused to the hyperfocal distance, which is twice the distance from PCAM to FlashCam, i.e. 32 m. The light paths of both, the stars (blue light path) and LEDs (red light path) can be seen in Figure 7, where they form the so-called "circle of confusion" (green light path) on the CCD plane. This circle is a criterion for acceptable sharpness. As a result of this procedure, stars and LEDs are defocused to the same degree. A slight defocusing makes spots cover more than one pixel and consequently allows a precise centre-of-gravity reconstruction of the spot position and keeps signals from saturation.

## 2.4 Pointing software architecture

As mentioned in the previous section, the images taken by PCAM are used to extract the pointing position of the telescope and the relative misalignment between the Cherenkov camera and the telescope's optical axis. This requires a solid image-processing software<sup>3</sup> framework, which is introduced in this section.

The process chart in Figure 8 describes the central steps and input/output of the pointing calibration software. The Telescope Control System (TCS) or image simulation

<sup>3</sup><https://gitlab.com/vaneldik/ctapointing>

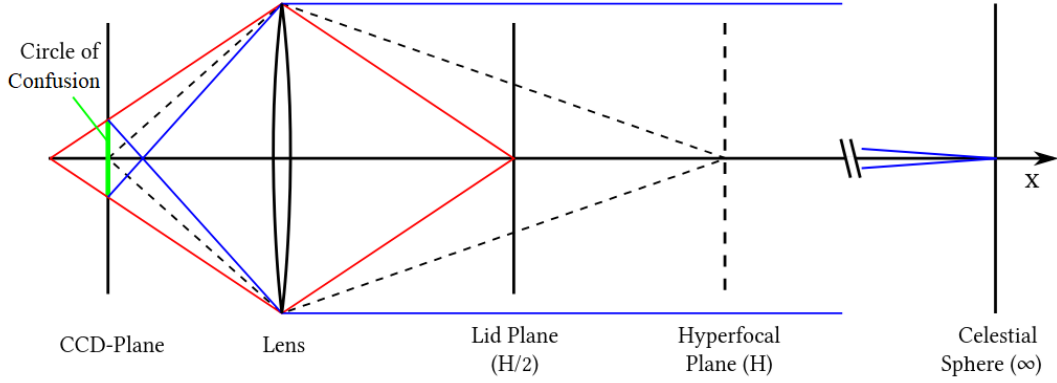


Figure 7: Light path scheme for PCAM. Red: light path for object on the Cherenkov camera, blue: path of star light, green: circle of confusion (a measure for acceptable sharpness), dashed black: hyperfocal plane and light paths for hyperfocal distance. Taken from Herpich (2010).

pipeline (both white) generate image data sets (light red) of a specific MST. For the purpose of simulation, the PCAM configuration, the Cherenkov camera configuration and a star catalog are given as input. The configurations contain information such as the camera geometry or orientation, nominal focal length and LED positions. Additionally, the analysis configuration delivers information about spot extractor as well as sky fitter and LED fitter. The configurations (light orange) and a star catalog (light purple) are provided to the pointing calibration pipeline (grey) which processes the image data sets in the following steps.

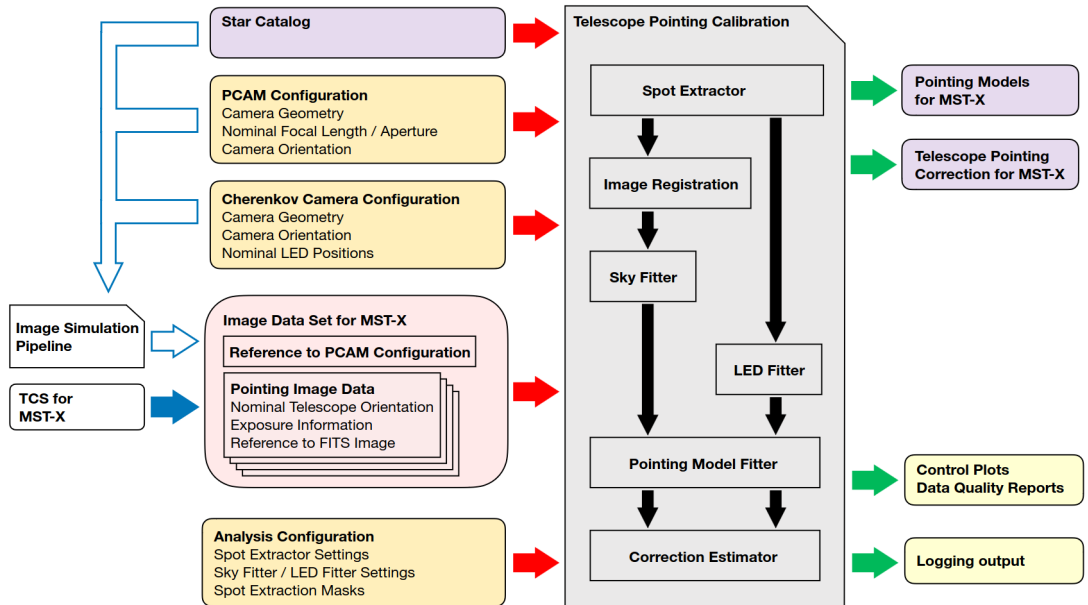


Figure 8: Scheme of the pointing calibration workflow. Taken from Garczarczyk (2022a).

Spots are determined by the spot extractor and pass the sky fitter (after an image registration step) or the LED fitter, respectively. The sky fitter correlates the PCAM pixels with sky coordinates. The LED fitter, which is the relevant fitting module in this thesis, delivers the position and orientation of the science camera. Pointing models and the telescope pointing corrections for the specific MST (light purple) represent the final output of the pointing calibration pipeline. Moreover, logging information is provided as well as control plots and data quality information (both yellow) to communicate problems to the TCS during run time (Garczarczyk, 2022a).

In this thesis the image data sets from PCAM (containing images and corresponding meta data like duration, exposure time or temperature) and the PCAM-, Cherenkov camera- and analysis configurations are used by the pointing calibration pipeline in order to extract the LED spots and reconstruct the LED positions. The software is implemented in a modular way, so that e.g. the output of the spot extractor can be saved externally in files or database and be reloaded as input of the LED fitter.

### 3 Preparatory measurements and considerations

The precision of LED position measurements with the final FlashCam-like set-up including 12 LEDs in circular arrangement is determined by reconstructing the LED spot positions and concluding the circle centre from a ring fit through these positions. A qualified position reconstruction can be done in case of stable thermal conditions, a correctly focused camera and suitable LED intensities, only. Therefore, these aspects are tested before constructing the final set-up.

#### 3.1 Thermal stability

As a thermal expansion of the PCAM chip influences the pointing accuracy, a cooling system stabilises the PCAM chip temperature to 5 °C for its application in the Atacama desert. The temperature of the laboratory is already stabilized sufficiently to enable the following measurements without extra cooling of the camera. To verify this, the camera temperature is recorded in two runs for 27 hours each, the results of which are plotted in Figure 30. The variation of the camera temperature does not exceed 1 °C including the initial warm-up and is less than  $\pm 0.1$  °C after stabilization.

#### 3.2 Focusing of the pointing camera

Successful focusing of the camera implies that stars and LEDs are focused (or defocused) in a similar way. A slight defocusing of the LEDs is a positive feature, because the LED spot is then spread over several pixels and hence its position can be determined to sub-pixel precision. For this purpose the camera is focused to the hyperfocal distance of 32 m as explained in section 2.3, so that stars and LEDs are blurred equally. Hence, PCAM is positioned at distance of 32 m with respect to the object which is supposed to be focused. To enable optical comparisons between different focus settings, existing elements in the laboratory such as dark plastic elements, squared paper and high-contrast letters are used. For the purpose of focusing, the PCAM housing is opened.

One defocused image and the sharpest image obtained are shown in Figure 9. The SAOImageDS9 software is used as image viewer for quick decisions on image quality. The objective setting is changed in equal steps for each new image which is controlled via a handmade scale (see Figure 10a). The focus ring is fixed by hot glue in the position which delivered the sharpest image (see Figure 10b), then the PCAM housing is closed. To verify the described manual focus approach, a dedicated night campaign on the ECAP rooftop is conducted. During this campaign, a significant increase in the detected number of stars is observed in comparison to campaigns conducted before the refocusing. (Eldik, 2024).

#### 3.3 Intensity adjustments

The spots of the LEDs in the final set-up are supposed to have intensity values and shapes similar to the stars exposed simultaneously. Night sky campaigns with an exposure time of 10 s showed maximum peak intensities of  $\approx 40000$  (in arbitrary units). Hence, this is also the desired intensity value for the LEDs at a 10 s exposure. The

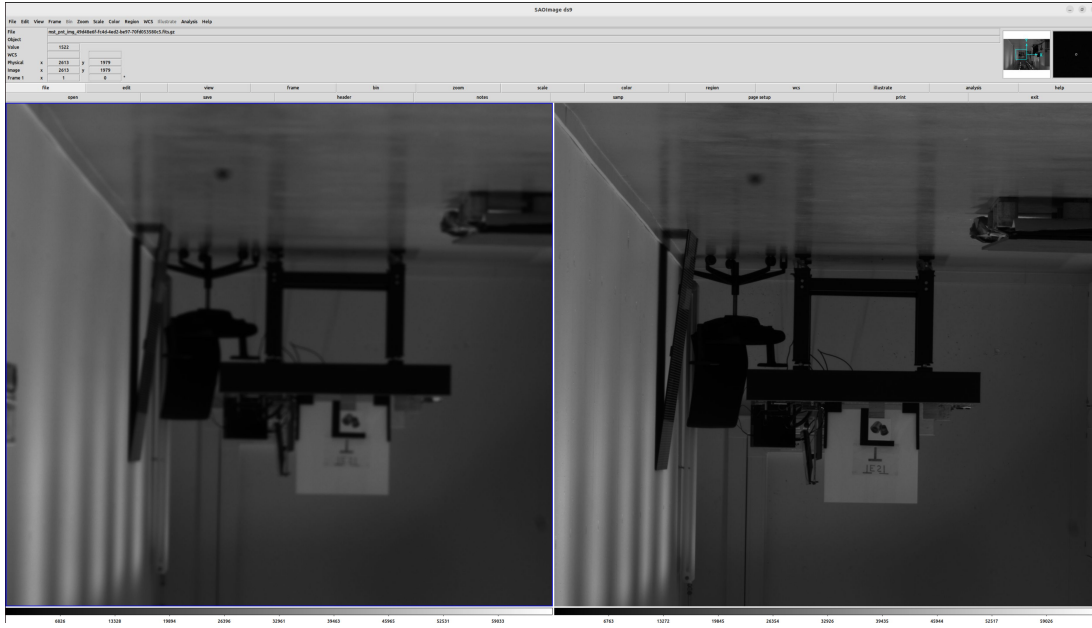


Figure 9: Images viewed via SAOImageDS9 before (left) and after (right) the focusing process. The letters and surrounding objects in front of the PVC board (bright square) on the optical table are focused on.



(a) The camera is focused with help of a handmade but sufficient scale to make objective settings easier comparable.



(b) The final setting of the focus, corresponding to the image in Figure 9 on the right side.

Figure 10: PCAM objective during the focusing procedure.

intensity maximum of a single pixel is  $65535^4$  so that a saturation of peak intensity values for high exposure times and/or high LED current is expected. Moreover, the minimum intensity is  $\approx 1000$  to provide a stable determination of the spot position, as detailed in section 3.3.1. This puts the desired intensity of 40000 well between both limits and provides a sufficient tuning range. In this chapter the intensities are controlled via two mechanisms: the adjustment of the LED current and the choice of suitable filters and a diffuser.

<sup>4</sup>derived from the 16-bit depth of the camera sensor counting from zero.

The relationship between LED current, exposure time, and spot intensity is measured and is explained in section 3.3.1. In addition, a diffuser is put in the beam path to obtain similar intensities over a larger beam width. The process of defining the best combination of filters and diffuser to achieve the desired attenuation is detailed in section 3.3.2.

The measurements shown in this chapter are performed with a fixed set-up using a red LED, which has been chosen for the purpose of MST pointing in previous testing series (SLI-343V8). This LED is set in a 3D printed pinhole mount which fixes the LED to a PVC plate. The LED, pinhole and PVC plate are shown in Figure 11. The LED current is controlled by a power supply in a range of 0 – 20 mA as defined for this LED in its data sheet, whereby the applied voltage is limited to 2.2 V.

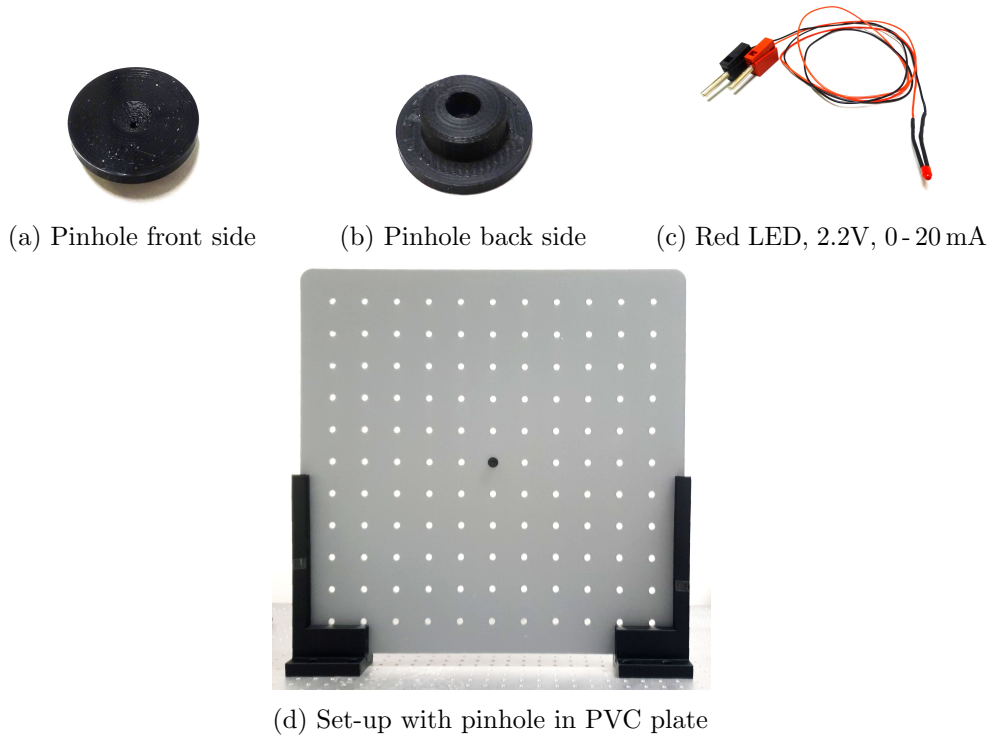


Figure 11: The pinhole fixes the LED to the PVC plate. The opening on its back side is customised to the size of this LED.

### 3.3.1 LED current

The LED is exposed for three different exposure times ( $10^{-2}$  s,  $10^{-3}$  s and  $10^{-4}$  s), each running through the adjustable LED current range in steps of 1 mA. The images are analysed using the CTA pointing software. The class `SpotExtractor` generates the container `spotlist` where the spot properties are stored. Information about flux, peak, variances, camera temperature, exposure duration, spot coordinates, rotation, focal length and other parameters is directly available via the `spotlist`. By plotting these variables their expected behaviour is verified. An example is given in Figure 12 where



the peak intensity values of the LED spot are plotted over the LED current range for the three different exposure times. Excluding saturation, an approximately linear behaviour (fitted according to the equation  $p(I) = a \cdot I + p_0$ ) for all exposure times is observable. The plot shows the expected intensity value range and approximately linear correlation between LED current and intensity. The quasi-linear behaviour matches the behaviour shown in the LED data sheet. The curve for the highest exposure time ( $10^{-2}$  s) shows the expected saturation.

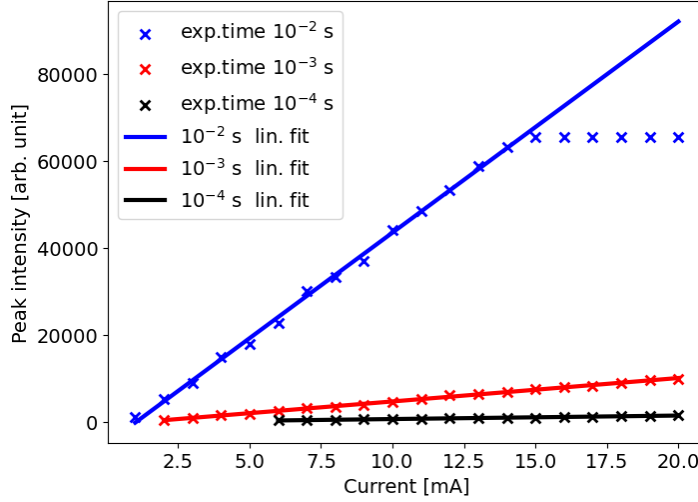
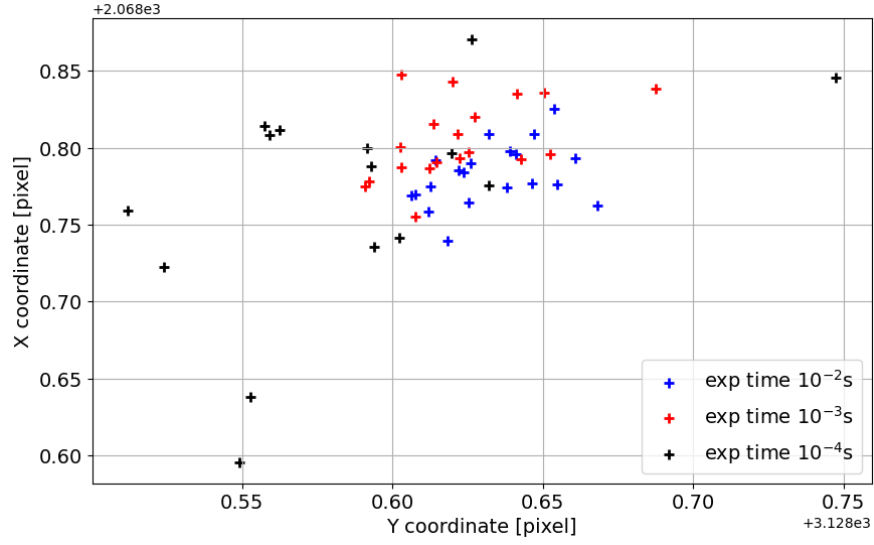


Figure 12: Peak intensities over LED current for the exposure times  $10^{-2}$  s,  $10^{-3}$  s and  $10^{-4}$  s with linear fits. Fit parameters are provided in Appendix A.1.

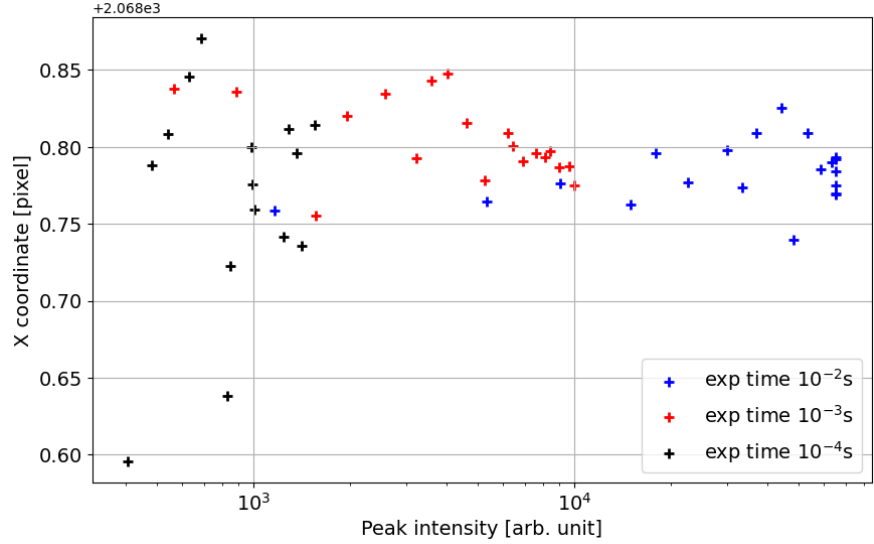
The acceptable lower intensity limit for a reliable determination of the spot positions can be determined from the same dataset. Figure 13a shows the spot positions for three exposure times. The variance is clearly increased for the shortest exposure time. Plotting the x-coordinate (vertical camera axis) of the derived spot positions as a function of peak intensity (see Figure 13b), the variance of the spot position exhibits a strong increase for intensities below 1000. Therefore, this threshold is used as minimum acceptable spot intensity. As one camera pixel covers about 15 arcsec, the determined spot positions for the lowest exposure time (black,  $10^{-4}$  s) are spread over about 4 arcsec on the x-axis and about 3.6 arcsec on the y-axis. The corresponding plot for the camera y-axis (horizontal camera axis) is shown in Appendix A.2 and exhibits an identical behaviour.

### 3.3.2 Intensity attenuation with filter and diffuser

As stated above, the expected intensity maximum of the stars is about 40000 for a 10 s exposure. The same intensity is achieved using the LED at a current of 10 mA, but with an exposure time of  $10^{-2}$  s which can be concluded from Figure 12. As the LEDs will be recorded in the same image as the stars (with exposure times in the range of 10 s), the intensity of the LED spots needs to be reduced by a factor of  $10^3$ . This cannot be done using the current control and, therefore, needs to be achieved by means of



(a) Extracted LED spot positions.



(b) Extracted LED spot x positions (vertical camera axis) over peak intensity.

Figure 13: X coordinate of the extracted LED spot positions as a function of (a) the Y coordinate and (b) the peak intensity for three exposure times:  $10^{-2}$  s,  $10^{-3}$  s and  $10^{-4}$  s. The intensity is varied using a LED current range of 0 – 20 mA for each exposure time. The plot for y axis is in Appendix A.2.

attenuating the LEDs' beam. For this purpose a set of ND filters with different Optical Densities (ODs) and a diffuser are tested in various combinations, see section 3.3.2. A filter holder, a new pinhole and an LED holder are 3D printed in order to arrange the filters and the diffuser in row to combine them on the optical axis.

The computer-aided design (CAD) sketch in Figure 14 illustrates the implementation: the LED (violet) is mounted in its customised holder (green), onto which two identical filter holders (blue) can be screwed. The whole assembly is then screwed to the pinhole (black). As its hole diameter and shape cannot be adjusted precisely by the 3D printer the hole is drilled (to the diameter of 1 mm) to obtain a circular hole shape and sufficient spot width. The letter "H" in Figure 14a marks the filter holder next to the hole, while "L" marks the one that is closer to the LED.

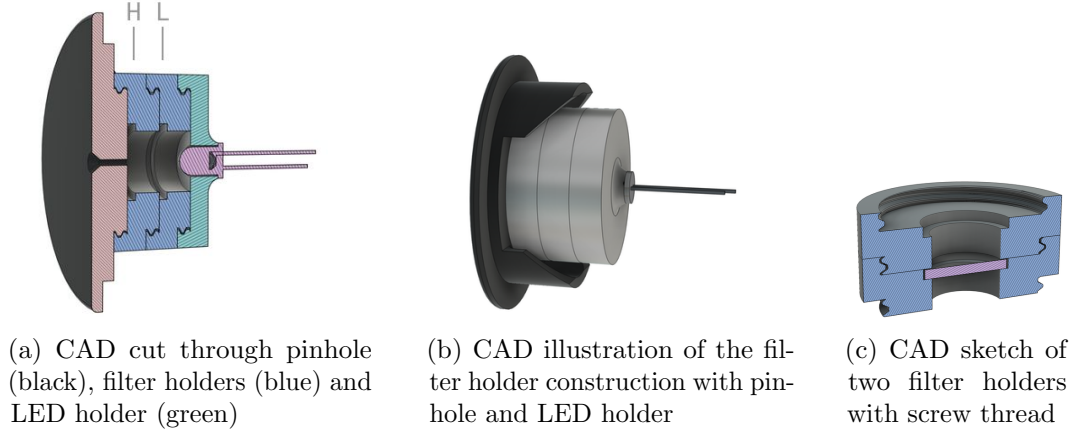


Figure 14: The updated LED mount houses two threaded holders facilitating quick changes of the ND filters and the diffuser.

A photo of the set-up can be seen in Figure 15: on the left hand side the 3D printed pinhole with the filter holders H and L and the LED holder, on the right hand side the box that serves to fix these holders.

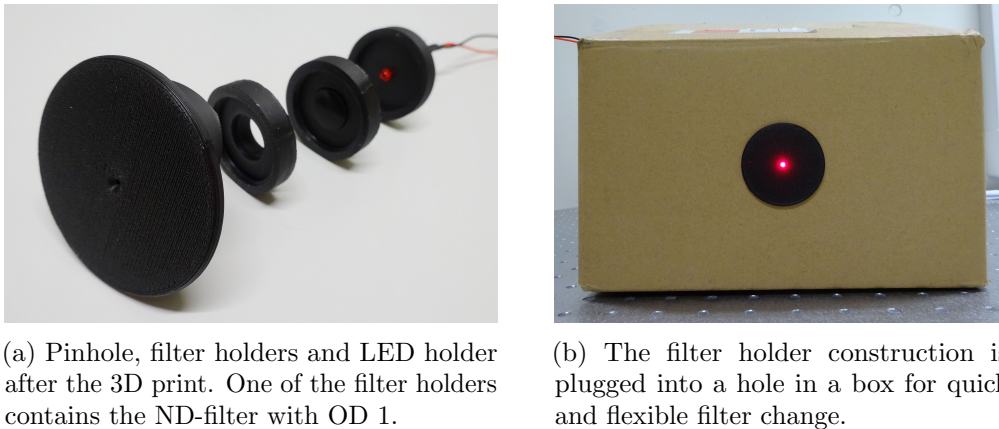


Figure 15: 3D printed holders and pinhole for the purpose of filter testing measurements.

The attenuation provided by the filters can be described via their optical density (OD): for OD  $x$  the light intensity is reduced to  $10^{-x}$  of its original intensity passing the filter. Putting several filters in series adds their respective optical densities, corresponding to a

multiplication of the transmission factors. The tested filters have nominal OD 1, 2 and 3. The light attenuation of the diffuser was previously unknown but could be determined to be about factor 100 by the results of the following measurements. Figure 16 shows an image of the diffuser and the filters.

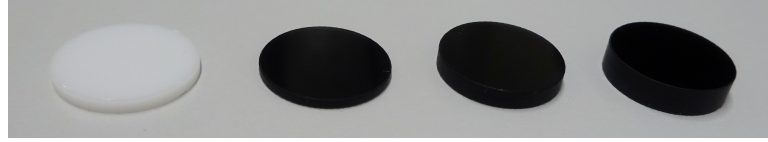
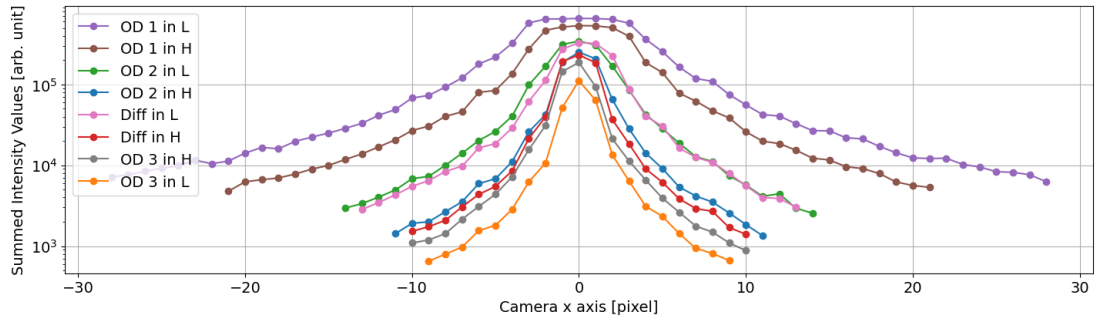
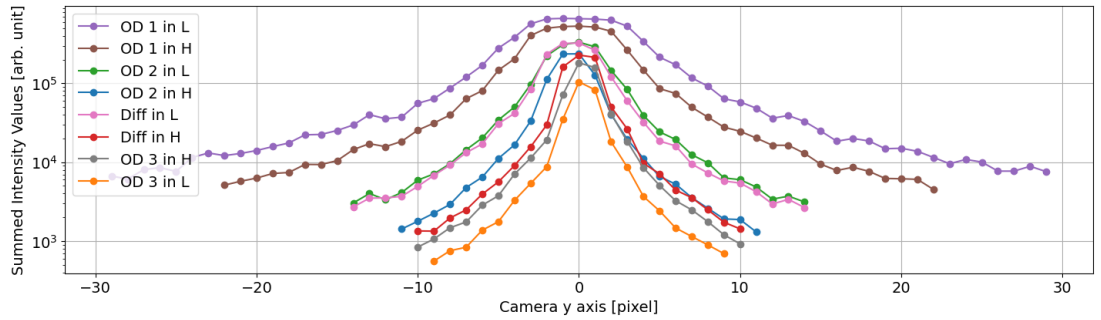


Figure 16: From left to right: diffuser, ND-filters with OD 1, 2 and 3

In the first step the filters and the diffuser are tested separately in the filter holders H and L each. The results are plotted in Figure 17: the intensities are summed over the y axis and projected on the x axis (Figure 17a) and vice versa (Figure 17b). As the images are taken with an exposure time of 5 s and an LED current of 10 mA the filter with OD 3 is the one that reduces the peak intensity to the desired value (image with OD 3 in L: peak intensity = 47521, orange curve in Figure 17). The other curves show up the more saturated pixels the higher their intensities are, which occurs in form of plateaus (best visible in the purple and brown curves for the filter with OD 1).



(a) Projection of pixel intensities on vertical camera axis (x).



(b) Projection of pixel intensities on horizontal camera axis (y).

Figure 17: Summed pixel intensity values for the LED spot (hole diameter 1mm, LED current 10 mA, exp. time 5 s). The spot radius is chosen three times the standard deviation. Filters with OD 1, 2 and 3 and a diffuser are tested in filter holder H and L.

As the shown intensity of about 47500 of the OD 3 filter in filter holder L (orange curve, see Figure 17) is already close to the desired value, a more detailed analysis of this spot is shown in Figure 18. The image size is cut at three times the standard deviation of the spot size based on the variance given by the `spotlist` parameter set. Gaussian fits (red curves) are applied to the projections corresponding to the fit equation

$$G(x) = A \cdot \exp(-((x - x_0)^2)/(2 \cdot \sigma^2)) \quad (1)$$

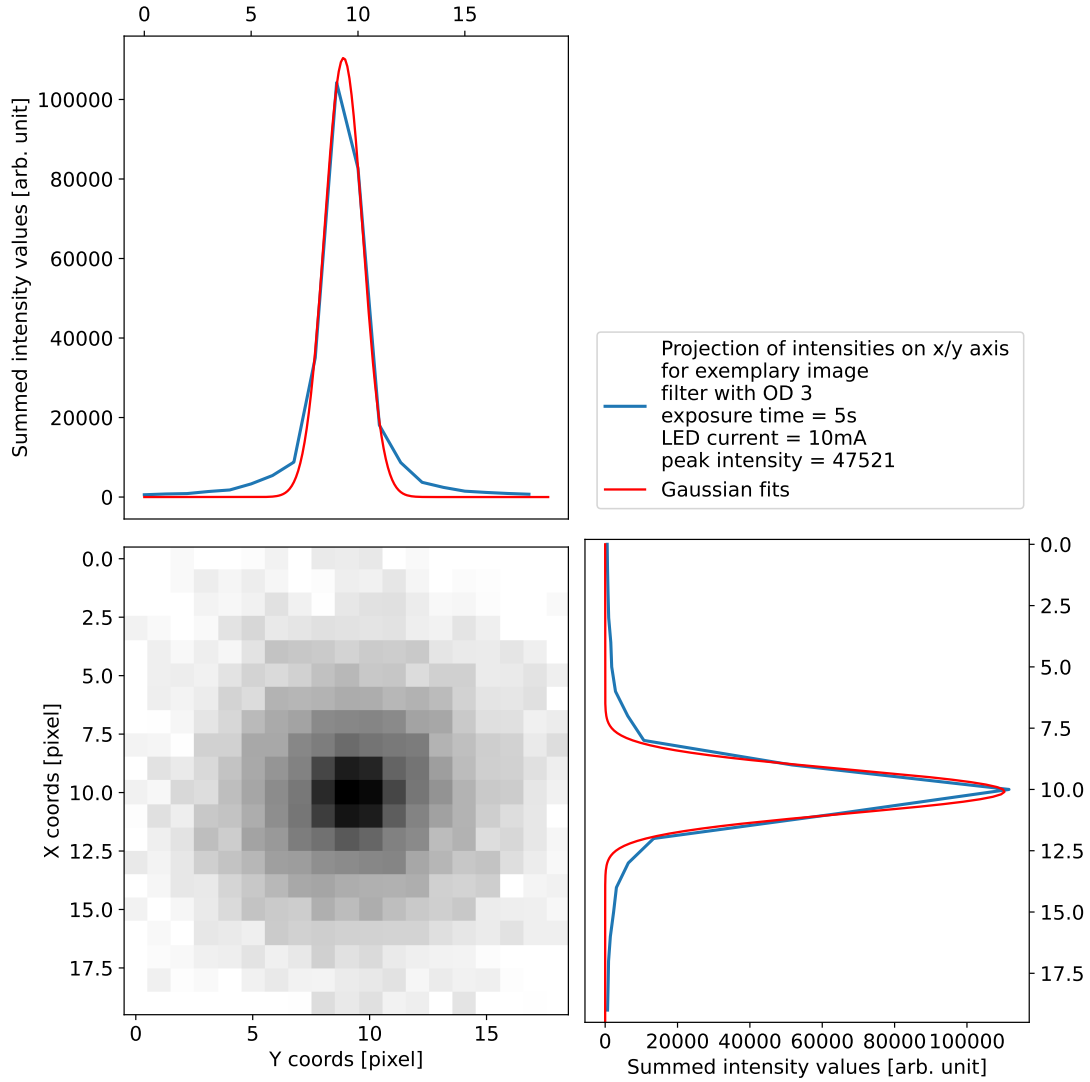


Figure 18: Extract of exemplary image from first filter test cut around the LED spot with radius of three standard deviations and summed pixel intensities projected on x- and y-axis, respectively. The filter with OD 3 is used for this image. The peak intensity is closest to the desired range of  $\approx 40000$  for this image.

The fit parameters (listed in Appendix A.3) indicate a symmetric circular shape of the spot. The standard deviation  $\sigma$  of the fit is used as a technical measure for the curve width to enable a detailed comparison between the spot shapes. Standard deviations of

$\sigma = (0.894 \pm 0.029)$  pixel for the projection on the y axis and  $\sigma = (0.900 \pm 0.024)$  pixel for the projection on the x axis are obtained. Visually determined from Figure 18 the spot covers about 6 – 7 pixels on both axes which is sufficient for a reliable position reconstruction. The diffuser is included with the intention to flatten out the angular emission profile of the LEDs. This avoids a substantial intensity reduction when the LEDs are mounted in a circle with an angles of about  $5^\circ$  to the optical axis in the set-up in section 4.

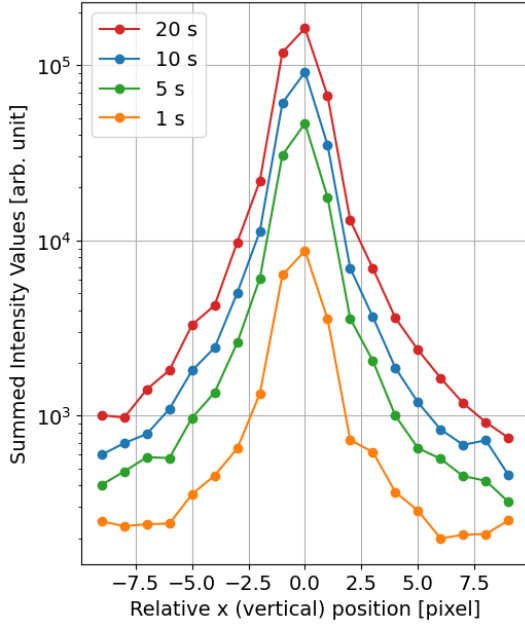
In addition, as can be seen in Figure 17, the OD 2 filter (green and blue curve) and the diffuser (pink and red curve) lead to a very similar reduction of intensity. The diffuser provides even a slightly higher attenuation than the filter if inserted in filter holder H nearby the hole. The spreading of the LED light caused by the diffuser attenuates the spot intensity to  $10^{-2}$  of its original intensity. As the optical density is additive, the diffuser in holder H can be combined with the OD 1 filter to obtain an attenuation corresponding to OD 3 or even a bit stronger. This configuration is expected to combine the homogeneous illumination and sufficient spot width provided by the diffuser with an adequate attenuation to achieve the desired illumination.

Two control measurements are performed to verify that the combination of diffuser and ND filter with OD 1 produces suitable spots. In the first series, the LED current is fixed at 10 mA while the exposure time is changed to 1 s, 5 s, 10 s and 20 s. These values are chosen as the exposure time to be used in CTA night sky campaigns is not defined yet, but is expected to fall in this range. The peak intensities are listed in Table 1 (left hand side). Peak evaluation is done akin to Figure 17 by summing intensities along one camera axis and plotting those sums over the other axis. This is shown in Figure 19a and 19b for the camera x and y axis, respectively. Here, the spot position from the `spotlist` set is subtracted, yielding a relative change with respect to the spot centre. The spot position remains the same for all chosen exposures. As the peak intensity of about 42000 for 10s exposure is closer to the desired value of 40000 than the result acquired with the single OD 3 filter (peak intensity of  $\approx 47500$  for 10 mA and 5 s), the combination of diffuser and OD 1 filter is considered superior.

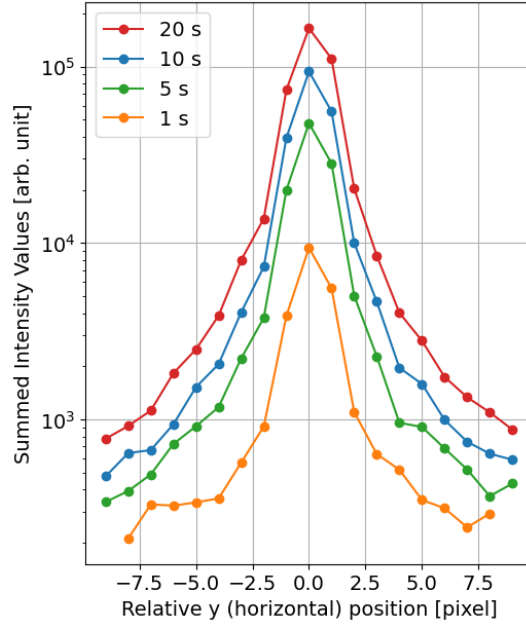
exp.time [s]	peak int. [arb. unit]	exp.time [s]	LED current [mA]	peak int. [arb. unit]
1	3908	5	20	44825
5	21443	10	10	41612
10	42022	20	5	37493
20	65513			

Table 1: Peak intensities using filter (OD 1) and diffuser. Left: The LED current is 10 mA. The desired peak intensity is obtained for 10s exposure. Right: The desired peak intensities are obtainable for all exposure times with suitable LED currents.

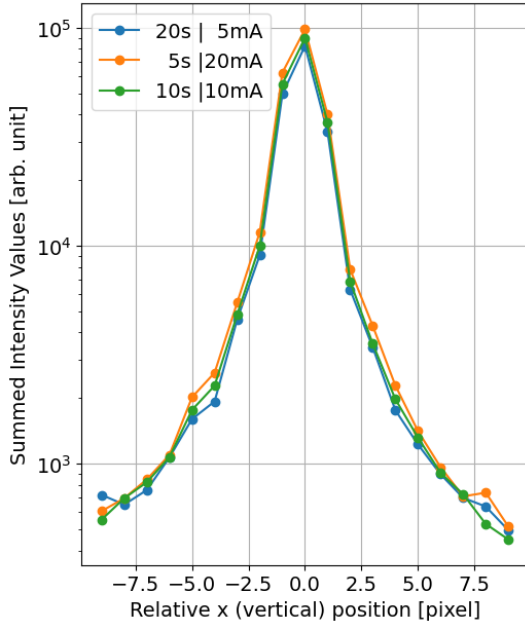
In a second test series, the exposure time and LED current are changed alternately as to keep the illumination about constant. The peak intensities are listed in Table 1 (right hand side). Evaluating the results in the same way as the first series, the plots shown



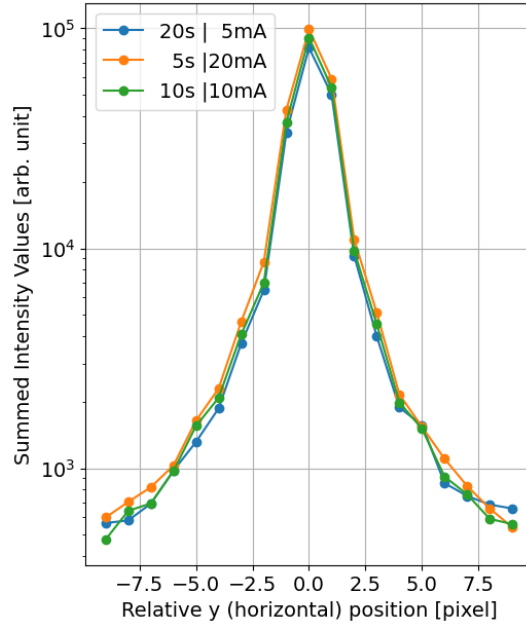
(a) Projection on vertical camera axis (x)



(b) Projection on horizontal camera axis (y)



(c) Projection on vertical camera axis (x)



(d) Projection on horizontal camera axis (y)

Figure 19: Summed peak intensity values for the LED spot (filter with OD 1 and diffuser, hole diameter 1 mm). The spot radius is chosen three times the standard deviation. For the plots in (a) and (b) the LED current is fixed at 10 mA. For the plots in (c) and (d) the exposure times and LED currents are adjusted so that similar peak intensities are reached (close to 40000). All values are listed in Table 1.

in Figure 19c and 19d are obtained. All three data sets yield virtually identical shapes. Figure 20 shows the spot with 10s exposure time (OD 1 filter and diffuser) plotted in

the same way as shown above in Figure 18 (OD 3 filter, 5 s) for better comparability. Here, the standard deviations obtained by the Gaussian fits are  $\sigma = (0.865 \pm 0.021)$  pixel for the projection on the y axis and  $\sigma = (0.872 \pm 0.021)$  pixel for the projection on the x axis. This indicates a circular shape of the spot. The spot covers 6 – 7 pixels again, so that the position reconstruction has a sufficient quality. This is consistent with the LED spot generated with the OD 3 filter shown above and fulfils the conditions concerning peak intensity and spot width. Additionally, the solution with the diffuser reduces intensity changes for a set-up with LED positions aside from the optical axis.

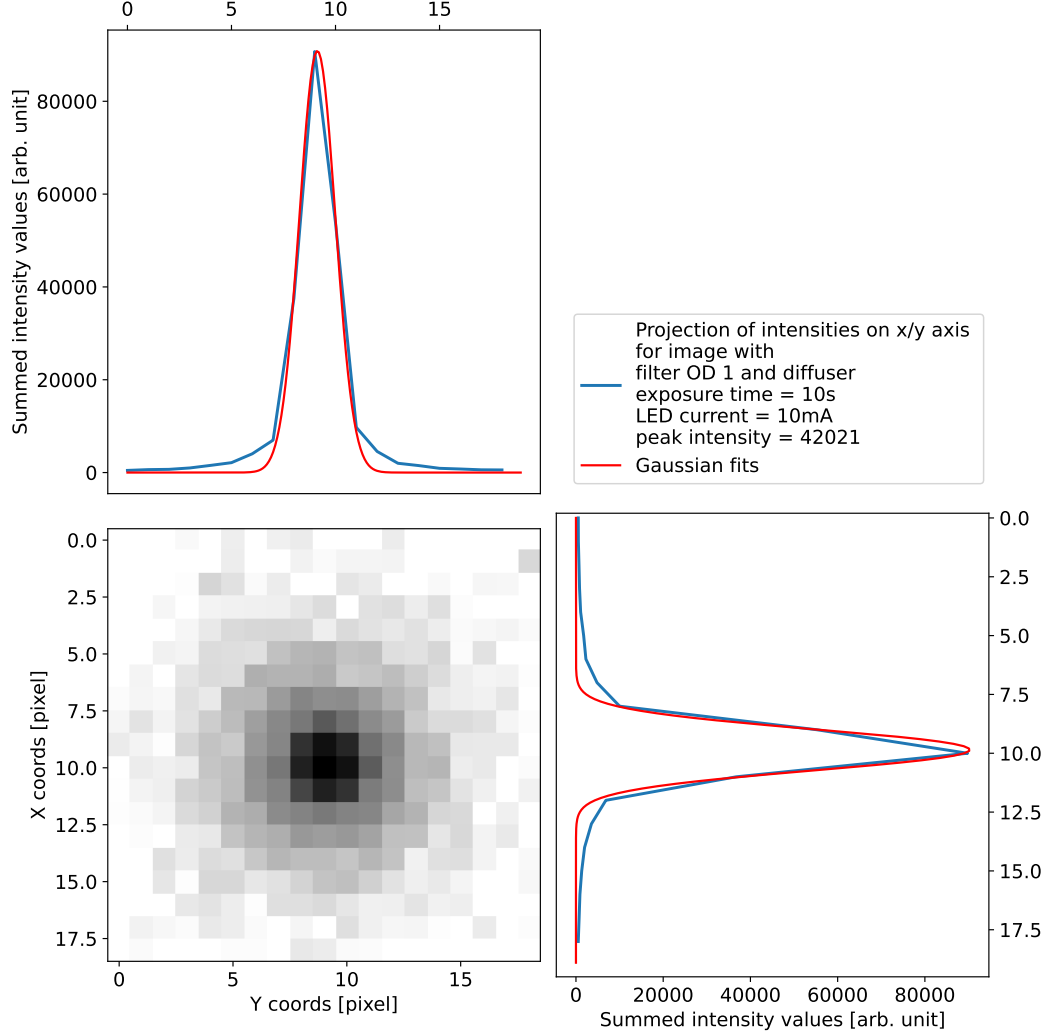


Figure 20: Extract of image with 10 mA LED current and 10 s exposure time cut around the LED spot with radius of three standard deviations and summed pixel intensities projected on x- and y-axis, respectively. A filter with OD 1 and a diffuser are used for this image. The peak intensity is  $\approx 42000$ .

Based on these final verification tests, the combination of diffuser and OD 1 filter is chosen for the consecutive set-up with a circular arrangement of twelve LEDs which is used to verify the pointing accuracy criterion and is discussed in the following chapter.



## 4 Verification of the pointing criterion using a FlashCam mock-up

The preliminary measurements shown in the previous chapter highlight the suitability of the LED, ND filter and diffuser combination. In this chapter, the scope of the set-up is expanded to also mimic the circular arrangement of twelve LEDs on the FlashCam. For the purpose of precise position adjustment of the LEDs on the mock-up of the FlashCam front, the combination of LED holder, filter holders and pinhole has to be updated and, hence, changed in size. As the output of LED light strongly depends on the distance between LED, filter, diffuser and pinhole as well as on the hole size, an adjustment is required. The first part of this chapter depicts the developed mock-up and its corresponding LED holder construction and the second part describes the readjustment of the pinhole size. Next, two image series are taken with this testing set-up and checked using basic variables such as the mean background or the camera temperature. Finally, the LED positions are reconstructed and a ring fit is performed to get the position of the circle centre. The precision of the ring fit is of fundamental interest concerning the pointing criterion and the applicability to the future MST configuration.

### 4.1 The FlashCam mock-up

As mentioned in section 1.2 and section 2.1, the pointing LEDs of FlashCam are positioned on a circle of radius of  $\approx 1.3$  m on their predefined positions. In order to achieve this geometry for the mock-up, an aluminum profile frame is constructed.

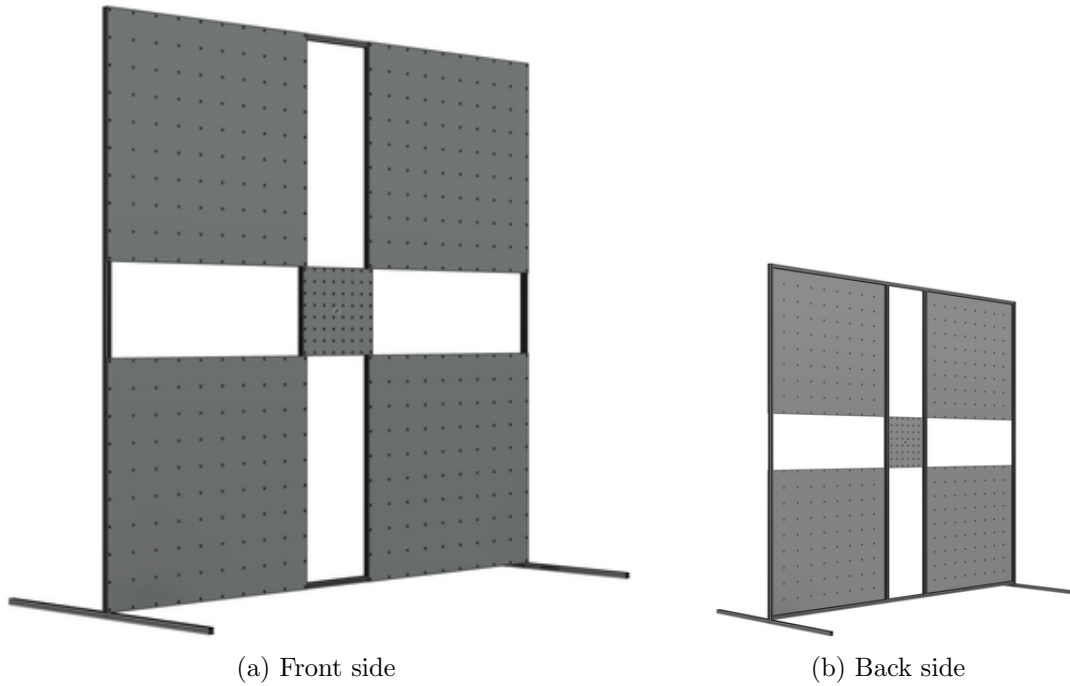


Figure 21: CAD design of the mock-up: an aluminum profile construction with PVC hole plates. The total size is about 250 cm  $\times$  260 cm.

To provide versatile mounting options, PVC boards are mounted on the aluminum profiles forming a wall of about  $2.50\text{ m} \times 2.60\text{ m}$ , strengthened by a wooden board in the back, see Figure 24b. Due to its size the construction is connected to the ceiling via a metal chain for stabilisation. The CAD sketch of the wall is shown in Figure 21.

The PVC plates are pervaded by a hole grid to mount twelve 3D printed base plates, each with a single filter holder set-up, as sketched in Figure 22c. Next, the pinhole sizes are adjusted as explained in section 4.2. To facilitate alignment, the filter holders are held to the base plates by means of two rubber bands, which allow for horizontal and vertical movement over several centimeters. An example of this assembly is shown in Figure 23. After the alignment, the filter holders are fixed to respective base plates with hot glue and the rubber bands are removed. The full set-up with twelve assemblies in a circle is shown in Figure 24.

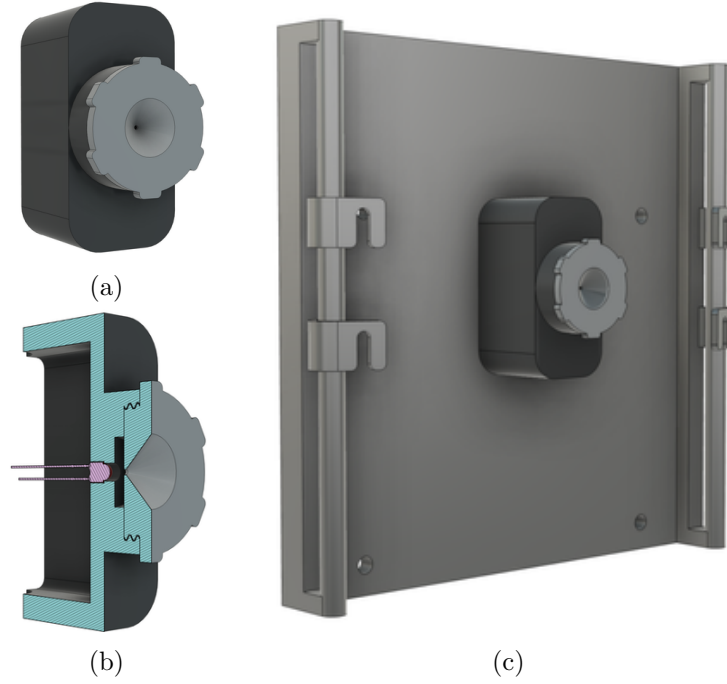
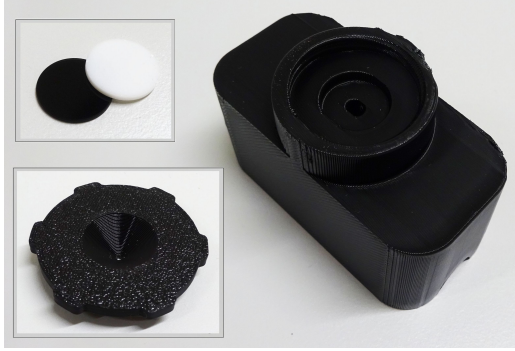


Figure 22: (a) and (b) show the final set-up of pinhole, filter holder and LED holder. The LED, filter, diffuser and pinhole are in direct contact. (c) shows the base plate with side bars. The filter holder construction is movable in two dimensions on the base plate via two rubber bands which are fixed by clips.

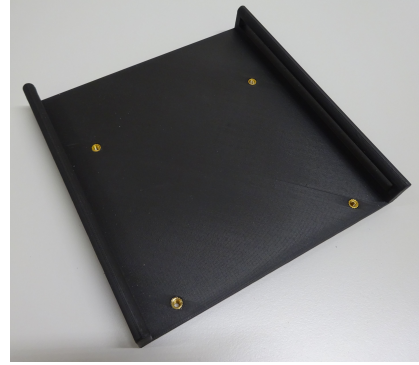
The sketch in Figure 22b highlights that the LED, filter, diffuser and pinhole are directly in contact without interspace which influences the output of LED light. The pinhole can be screwed into the LED holder, securing the filters mechanically.

## 4.2 Optimisation of the pinhole size

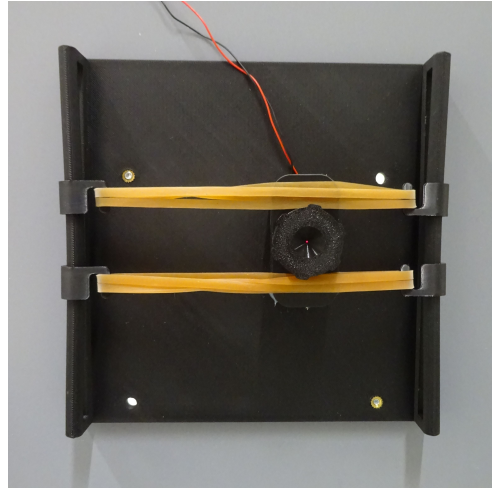
First tests of the new LED assembly using the 3D printed pinholes show vastly varying, mostly too low intensities. Trials with drilled holes of  $1\text{ mm}$  diameter provide only



(a) 3D printed filter holder set-up with diffuser, ND filter (OD 1) and pinhole which keeps the filter and diffuser inside the holder.



(b) The 3D printed base with inserted threads can be fixed to the PVC plates by screws.

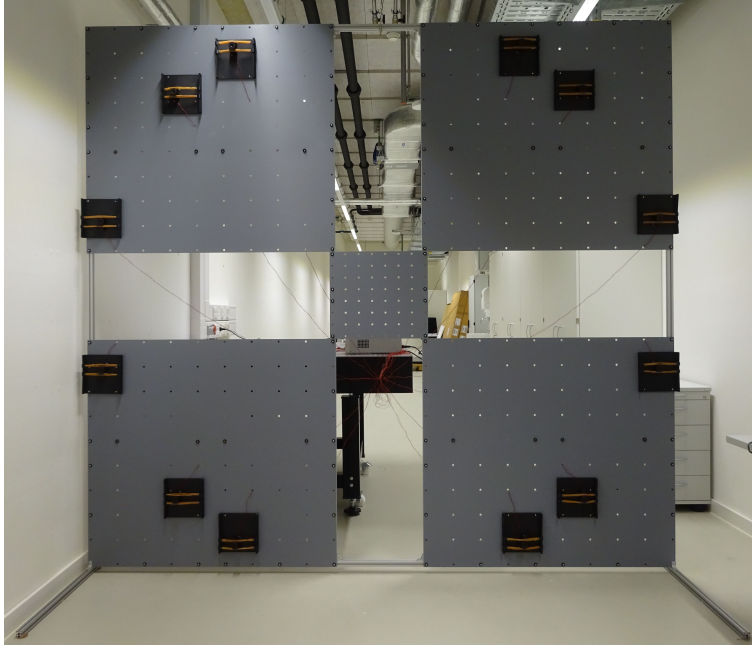


(c) The final positioning construction for one LED contains a base plate and a filter holder with pinhole, clips and rubber bands.

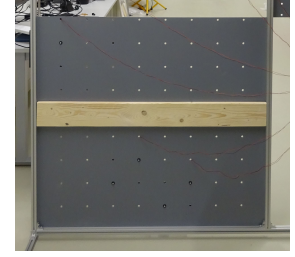
Figure 23: The flexible mounting of the LED and filter holder on its base allows a precise adjustment of the LED position. The filter and diffuser are exchangeable. The pinhole keeps them inside their holder and is fixed by a screw thread.

saturated peak values. Inspection of the 3D printed holes by microscope, as shown in Figure 25a, reveals that the printed holes are mostly not circular in shape and partially blocked by residual printing support material.

As a solution, the 3D printed pinholes are shaped using a hot wire of 0.5 mm diameter. This creates holes of good quality as verified under the microscope again (Figure 25b). 19 pinholes are created, their respective diameters are listed in Appendix A.5 together with the obtained peak intensities. The respective measurement is performed akin to the description in section 3.3 where the filters and diffuser are tested. The new filter holder assembly is placed on the optical axis of PCAM with a distance of 16 m and fixed by a box corresponding to Figure 15b. The mean diameter of the pinholes is  $(0.519 \pm 0.010)$  mm. Each pinhole is analysed via the spot imaged by PCAM. The

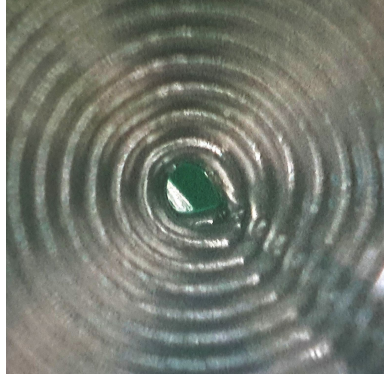


(a) The LEDs are in their final positions on the front side of the mock-up.

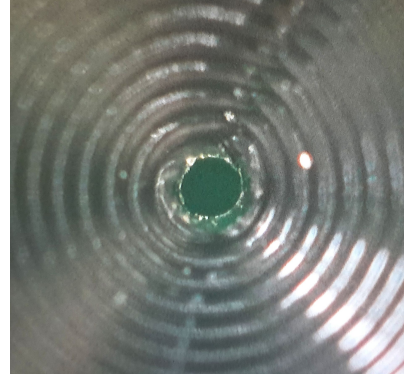


(b) The back side of the mock-up has to be supported by a board.

Figure 24: The final set-up with twelve LEDs in the circular arrangement imitates the FlashCam front.



(a) The 3D printed holes are deformed and not precisely circular. Support material blocks the hole.

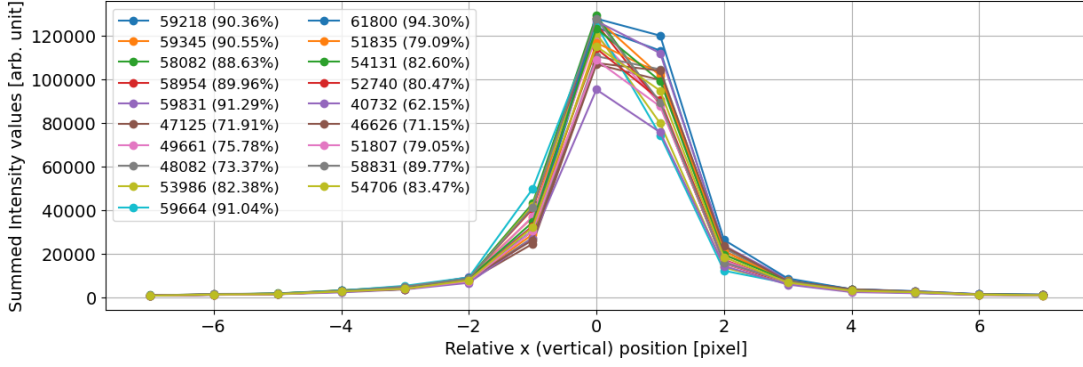


(b) The holes are brought to a circular shape and support material is removed by a 0.5 mm hot wire.

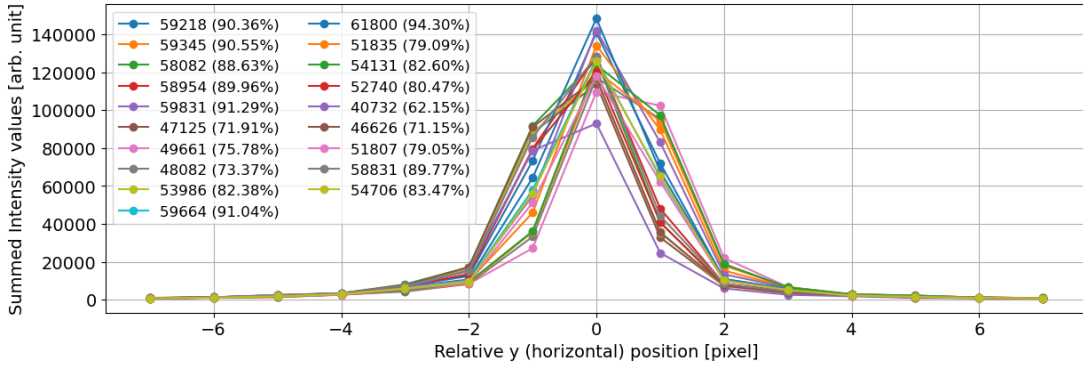
Figure 25: The adjustment of a proper hole diameter is performed under a microscope.

projections of the 19 spots on the x- and y-axis, respectively, are shown in Figure 26. The legend lists the respective peak intensity and saturation rate which is calculated via the fraction of peak intensity over saturation value.

The now reduced width of the pinholes results in spots covering 4 – 5 pixels, compared to 6 – 7 pixels for the previously used 1 mm holes. This width is still sufficient for a reliable position reconstruction. In order to achieve rather uniform illumination, the



(a) Projection of summed pixel intensities on vertical camera axis (x).



(b) Projection of summed pixel intensities on horizontal camera axis (y).

Figure 26: Summed pixel intensities for the LED spot with filter (OD1) and diffuser. The method is outlined in Figure 18. The exposure time is 10s, the LED current is 10 mA. The hole diameter of 0.5mm is melted into 19 pinholes. The peak intensity and saturation value are given in the legend for each hole.

pinhole providing lowest intensity and the six pinholes with highest intensities are discarded. Twelve pinholes with spot peak intensity values in the range of 46000 to 58000 remain. Next, the pinholes are screwed into the filter holders and the set-up is completed as described in section 4.1 by position alignment and hot glue fixing.

### 4.3 Analysis of the set-up stability

For the following analysis, the LEDs are numbered counter clockwise as depicted in Figure 27. The x- and y-coordinate of the nominal position for each LED (Eldik (2024)) are given in mm with respect to the nominal circle centre.

Two series of images are taken with identical exposure time of 10 s and LED current of 10 mA, with each series spanning 27 h and containing 327 and 324 images, respectively. The second series starts 10 days later, during which the LEDs are kept running. For each series, the first image is discarded due to large deviations in all evaluated parameters such as position and flux. The image series are analysed concerning the parameters peak, flux, camera temperature, mean background, focal length and rotation to verify the stability of the set-up.



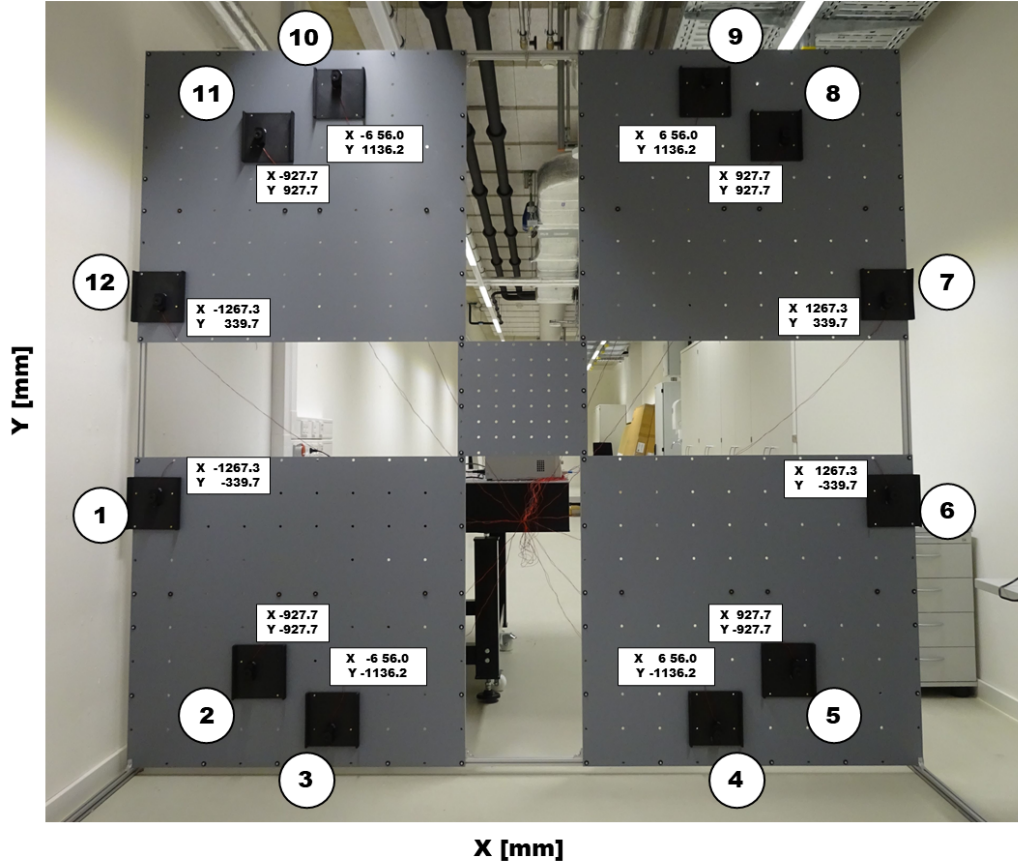


Figure 27: The numeration and positions of the LEDs serve for their identification in plots. All LED positions are determined to sub-millimeter precision by the FlashCam design.

Figure 28 shows the results for peak intensity and flux values. As expected the peak intensities are lower in the final set-up than in the preparation images in Figure 26 because the LEDs do not point directly into the camera. In section 3.3.2 the diffusers are chosen in order to reduce attenuation issues due to LED positions aside the optical axis. Although the diffuser provides a more isotropic illumination, a certain directivity is still to be expected, but the intensity reduction is lower than without the diffusers. The LEDs are mounted on the PVC wall with a radius of about 1.3 m, the distance between wall and PCAM is about 16 m, so the camera receives the LED light under a  $5^\circ$  angle. The peak intensities take values from 45000 down to 20000. In spite of this intensity reduction, reliable position reconstructions can be performed, as none of the LEDs have intensities below 1000 (compare section 3.3.1). For the purpose of this lab experiment the measured peak intensities are within the usable range and could be fine-tuned by the LED current if necessary. It should be mentioned that the intensity of LED 12 is visibly lower compared to the other LEDs (especially in the first image series) which implicates some consequences on the position variable that will be subject to the discussion in section 4.4.2.

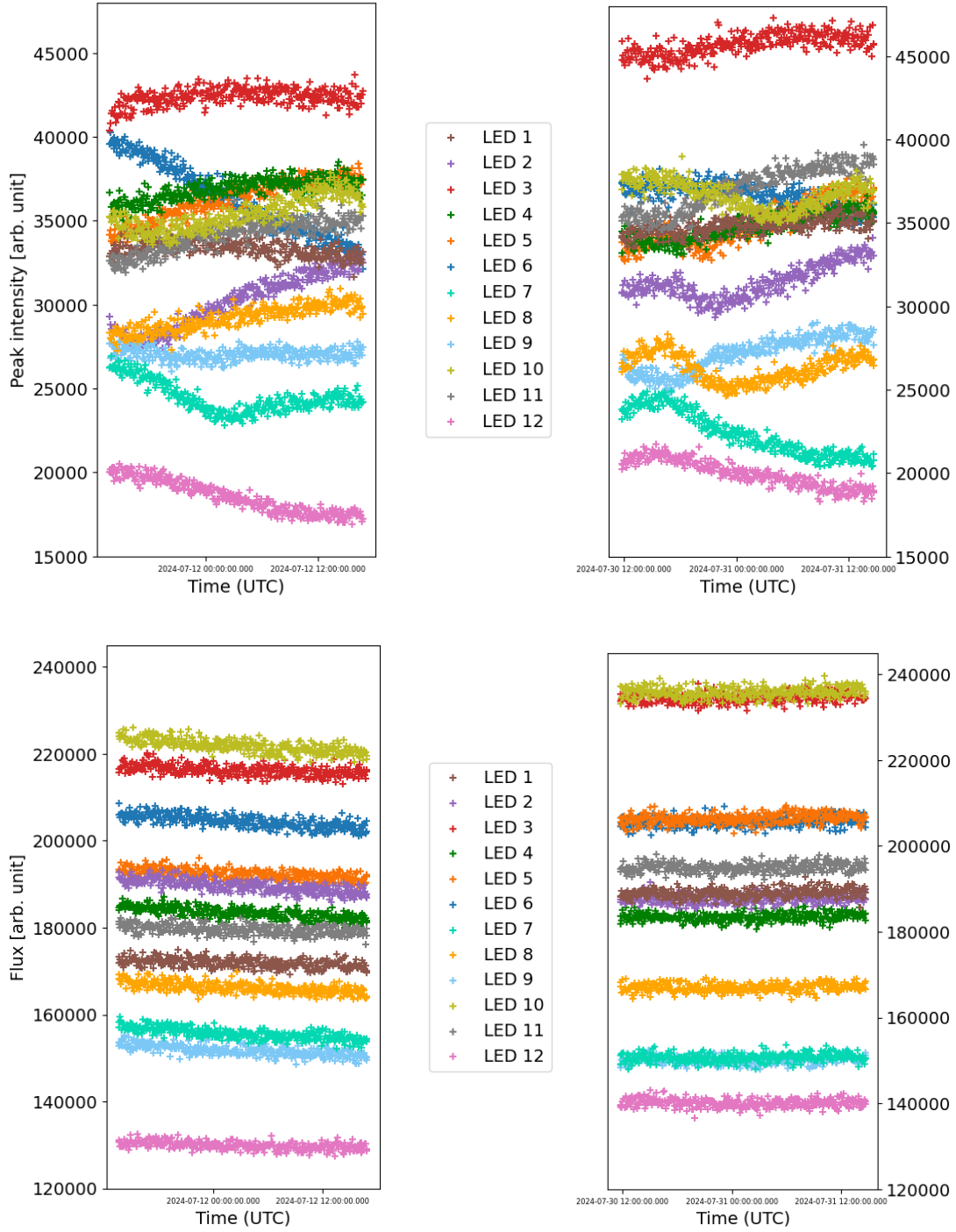


Figure 28: LED peak intensity values (top) and LED fluxes (bottom) for 326/323 images (exp. time 10 s, current per LED 10 mA, each LED with diffusers and OD 1 filters) over 27 hours each series. Left: first series, right: second series 10 days after the first.

As the first campaign has been started some hours after constructing the set-up, only, it is expected that settling effects are visible in the `spotlist` variables of this

campaign. The LEDs are not turned off during the ten days between the image series. From previous studies it is known that the LEDs decrease slightly in intensity during the initial operation time. Figure 28 confirms the assumption that the LED fluxes slightly decrease during the first campaign. After the ten days between the series the fluxes have leveled off and are constant over the 27 hours of measurement. For six of the twelve LEDs the flux increased between the first and the second campaign. Reasons for this behaviour are not obvious, so temperature and background are analysed with respect to stability in the next step. Besides, it cannot be excluded that the laboratory was entered by other persons which may have caused slight changes in the measurement conditions.

The mean background is plotted in Figure 29 and looks very similar for the first and second campaign. The mean value is  $(12.89 \pm 0.28)$  in arbitrary units (to be compared to intensity values) for the first series and  $(12.87 \pm 0.28)$  for the second series. The mean background can be assumed as constant. Besides, the background intensity values are very low considering peak intensity values in the range of  $10^4$ . The background is subtracted from the spot intensities by the software.

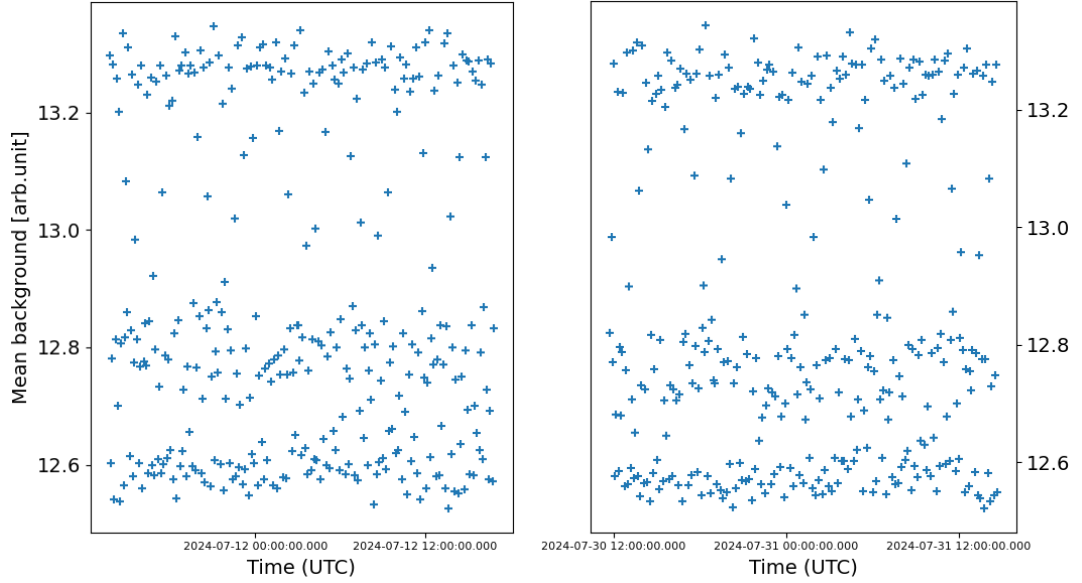


Figure 29: Mean background for 326/323 images (exp. time 10s, with diffusers and OD 1 filters) over 27 hours each series. Left: first series, right: second series 10 days after the first.

Temperature changes of the camera affect the measurements. As the laboratory temperature is stabilized to  $\pm 1^\circ\text{C}$ , the effect should be minimal. The temperature of the camera is shown in Figure 30 for both series. After an initial warm-up phase, the camera temperature is stable within  $\pm 0.1^\circ\text{C}$ . The mean temperature is  $(22.458 \pm 0.018)^\circ\text{C}$  for the first and  $(22.74 \pm 0.03)^\circ\text{C}$  for the second image series, where the rising tail is neglected. No effect on the measurement is expected during each series.



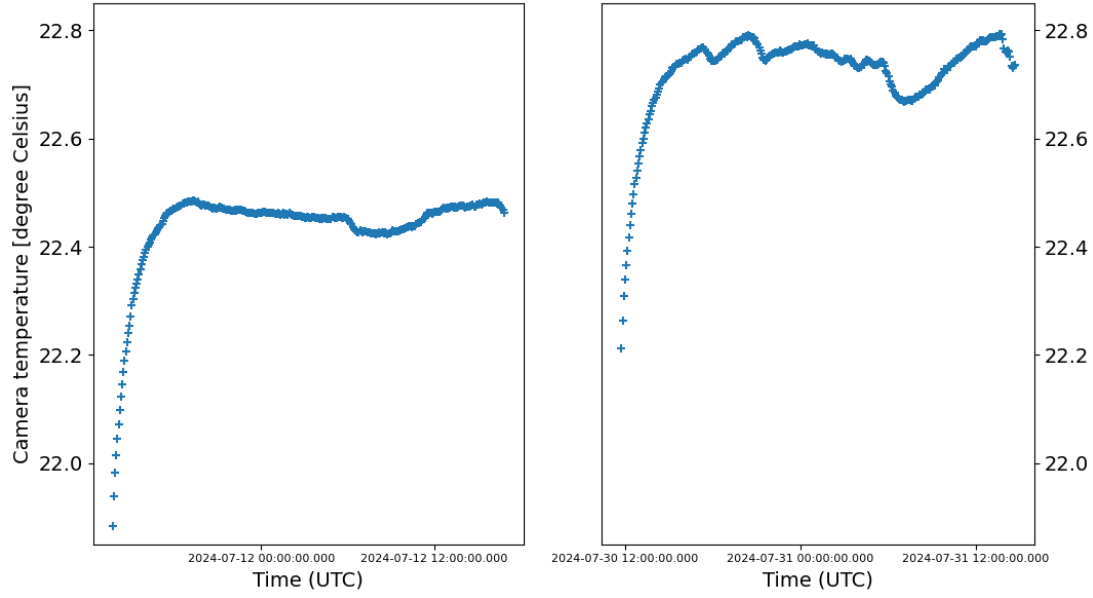


Figure 30: Camera temperature for 326/323 images (exp. time 10s, with diffusers and OD 1 filters) over 27 hours each series. Left: first series, right: second series 10 days after the first.

In addition, the distance between PCAM and Cherenkov camera, given as focal length of the Cherenkov camera, is calculated by the CTA pointing software and plotted in Figure 31. The software calculates the focal length using the fitted LED circle and

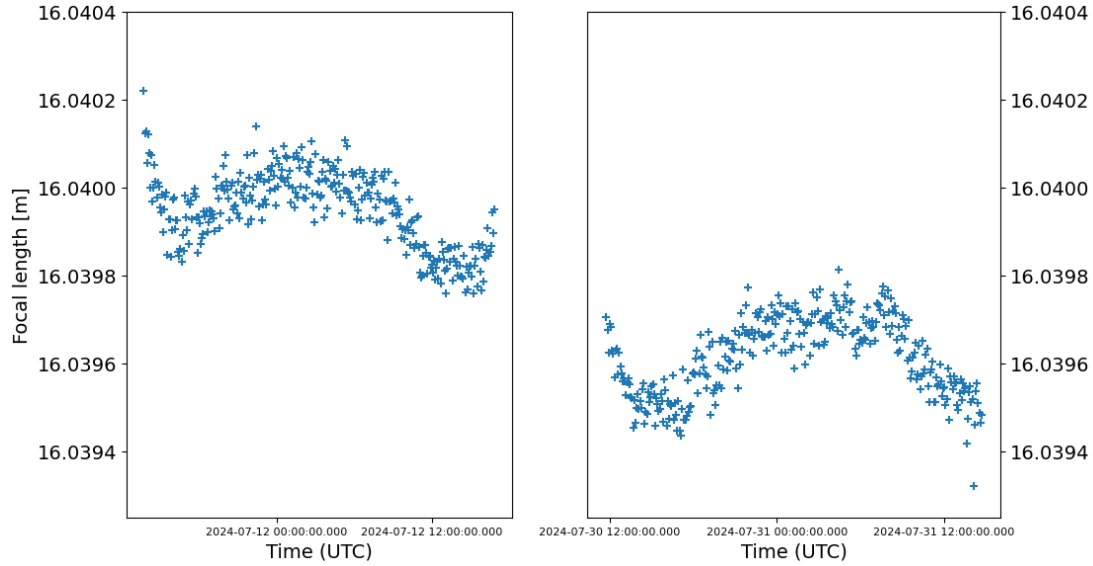


Figure 31: Focal lengths of FlashCam (representing the distance between PCAM and FlashCam) for 326/323 images (exp. time 10s, with diffusers and OD 1 filters) over 27 hours each series. Left: first series, right: second series 10 days after the first.

the camera properties of PCAM and FlashCam. A certain decrease over time can be derived from the both curves, but the over all changes are neglectable. The mean value is  $(16.039\,95 \pm 0.000\,09)$  m for the first and  $(16.039\,62 \pm 0.000\,09)$  m for the second image series. The nominal focal length is 16 m.

The rotation of the fitted circle is given with respect to the horizontal axis of the PCAM chip. The two diagrams on the top of Figure 32 show the achieved rotations for both series. A centered running average is plotted in red and subtracted from the

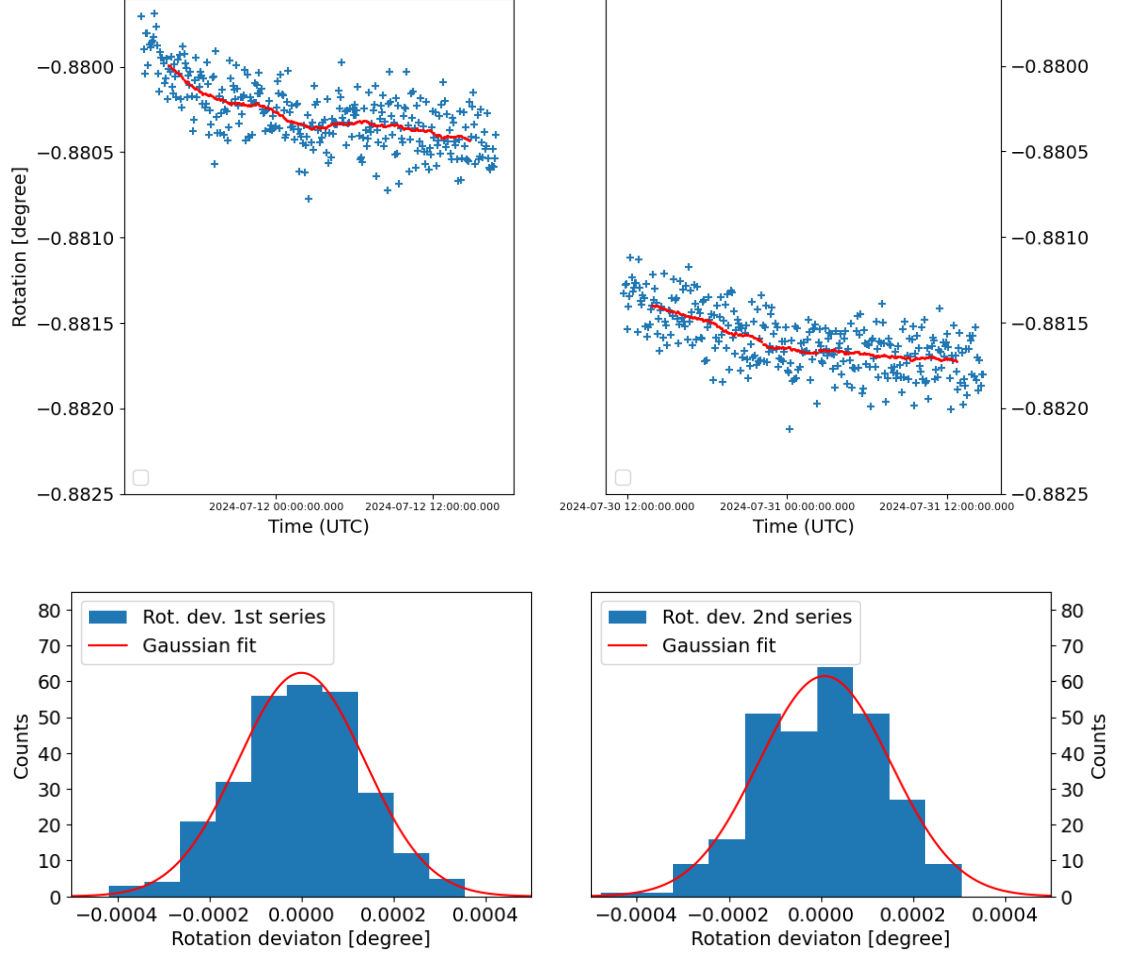


Figure 32: Top: Rotations for 326/323 images (exp. time 10 s, with diffusers and OD 1 filters) over 27 hours each series. Bottom: Histograms of the rotation deviations from the corresponding running averages. Left: first series, right: second series 10 days after the first.

rotation values. The obtained rotation deviations are plotted as histograms in the bottom diagrams of Figure 32. The widths of the Gaussians fitted to those distributions are given by  $\sigma = (1.38 \pm 0.06) \times 10^{-4}$  deg for the first series and  $\sigma = (1.44 \pm 0.13) \times 10^{-4}$  deg for the second series. Hence, the rotation deviation angles are in the sub-second range and can be neglected.

From the constant behaviour shown in the plots in Figure 29, 30, 31 and 32 the conclusion can be drawn that mean background, camera temperature, focal length and rotation do not affect the positions of the LEDs.

#### 4.4 Time-dependent analysis of the LED positions

With the stability of the set-up now verified, the campaigns are evaluated concerning the LED positions in vertical and horizontal direction. First the change of the determined LED positions with time is evaluated. The centre of the LED circle is found by a ring fit for both campaigns. The position deviations of the LEDs and achieved centres are shown as histograms. From this step conclusions on the precision of the camera centre determination in the applied pointing method can be drawn.

##### 4.4.1 Movement of LED positions

For both campaigns the LED positions are plotted after subtraction of the second image (as a reminder the first image had to be excluded, see section 4.3) to get the relative change of the LED positions over the 27 hours of measurement. The positions on the vertical camera axis are shown in Figure 33, the positions on the horizontal camera axis can be seen in Figure 34.

The curves are labeled in arcsec and mm (projected on the FlashCam front). The pixel values are converted to arcsec values via the `pixel_angle` conversion factor of 15.51 arcsec/pixel. This factor is calculated by the software based on the focal length of 50.0 mm and pixel size of 3.76  $\mu\text{m}$  of the ZWO ASI2600MM Pro given by the camera configuration file following the equation

$$\text{position [arcsec]} = \frac{3.76 \mu\text{m}}{50.0 \text{ mm}} \frac{180}{\pi} \cdot 3600 \cdot \text{position [pixel]} \quad (2)$$

$$\approx 15.51 \cdot \text{position [pixel]}. \quad (3)$$

The arcsec values are converted to mm by the use of the fitted focal length ( $\approx 16.040 \text{ m}$ ) of the FlashCam:

$$\text{position [mm]} = \frac{1}{3600} \frac{\pi}{180} \cdot \text{focal length [m]} \cdot 1000 \cdot \text{position [arcsec]} \quad (4)$$

$$\approx 0.07776 \cdot \text{position [arcsec]} \quad (5)$$

For both calculations the small-angle approximation ( $\tan \alpha \approx \alpha$ ) is used as the angles are in the range of about 1 arcsec. For the purpose of visualisation the curves for the LEDs are shifted by 1 arcsec each, relating to the previous one. The science camera centre positions are determined by a ring fit through the twelve LED positions following the standard implementation of a maximum likelihood fit (the expected LED positions are minimised against the determined LED positions). They are plotted in black in Figure 33 and 34. A centred running average curve is plotted for each LED in black and for the camera centre in white, each with a window of 20 entries.

A negative slope for all LED positions on both axes can be stated, that means a shift of the LED positions downwards and to the left (view from PCAM to LED board). This is assumed to origin from a deformation of the material (a rather soft and flexible PVC plate) as the temperature is excluded as influencing factor. The slopes in the second campaign are clearly flatter. Obviously the set-up has settled to a certain

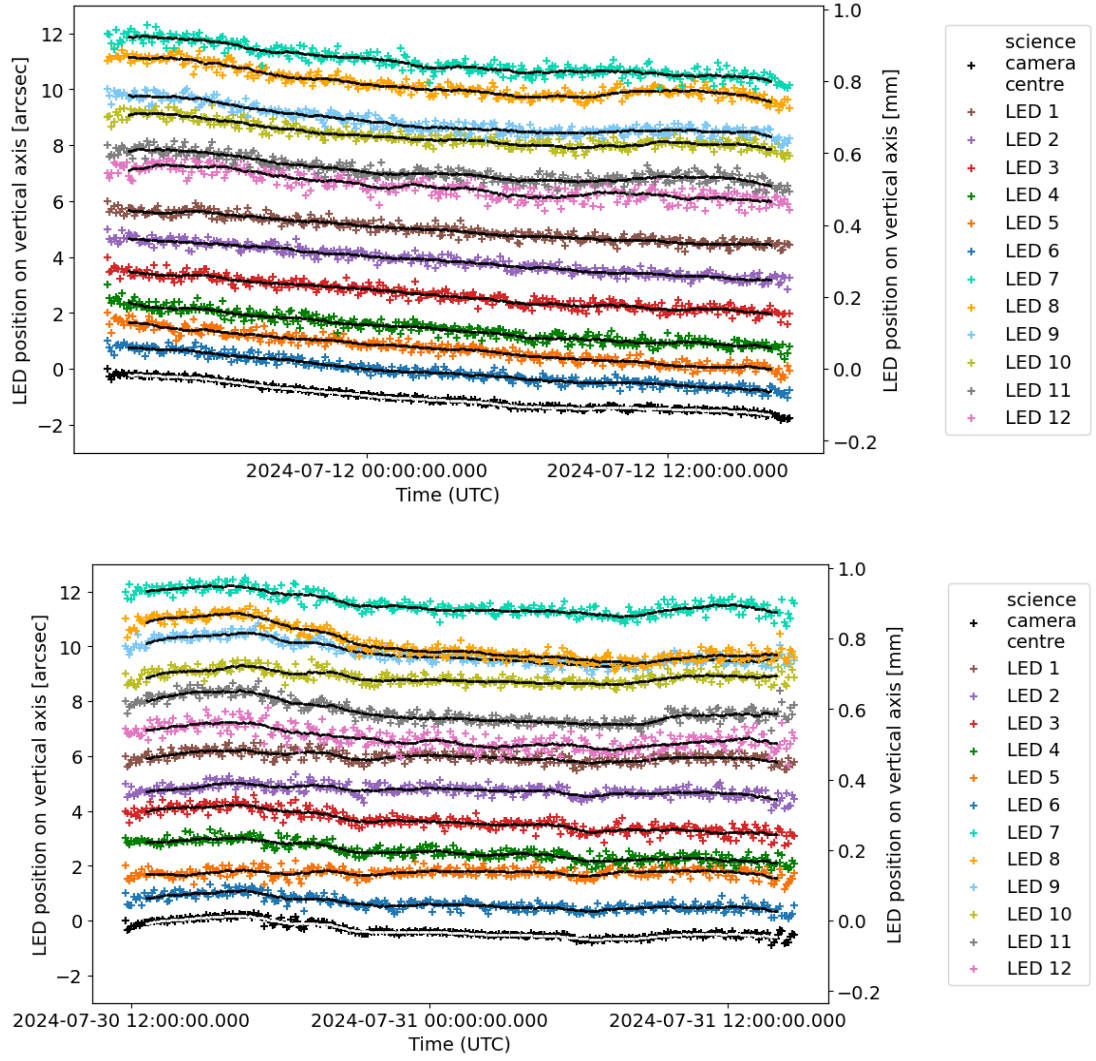


Figure 33: Vertical positions of the twelve LEDs and of the science camera centre (black data points) for the first campaign (top) and second campaign (bottom) are plotted. The first image of the current campaign is subtracted, then each of the curves is shifted on the y-axis by 1 arcsec relating to the previous one for visualisation. The running averages are plotted as black (white) lines.

extent during the ten days between the campaigns. In spite of the wobbly PVC plates, the wooden support boards and a flexible aluminum frame the position changes of the LEDs over 27 h are about few arcsec, only. In vertical direction the change is  $\approx 1$  arcsec for the first series and  $\approx 1.5$  arcsec for the second series, in horizontal direction it is  $\approx 2.5$  arcsec and  $\approx 4$  arcsec, respectively.

The discussed diagrams in Figure 33 and 34 give no hint at the behaviour of the position changes over the entire measurement duration of ten days. For this purpose, the starting image of the first campaign is subtracted from the other images of both campaigns to make them comparable. Then the movement of the science camera centre

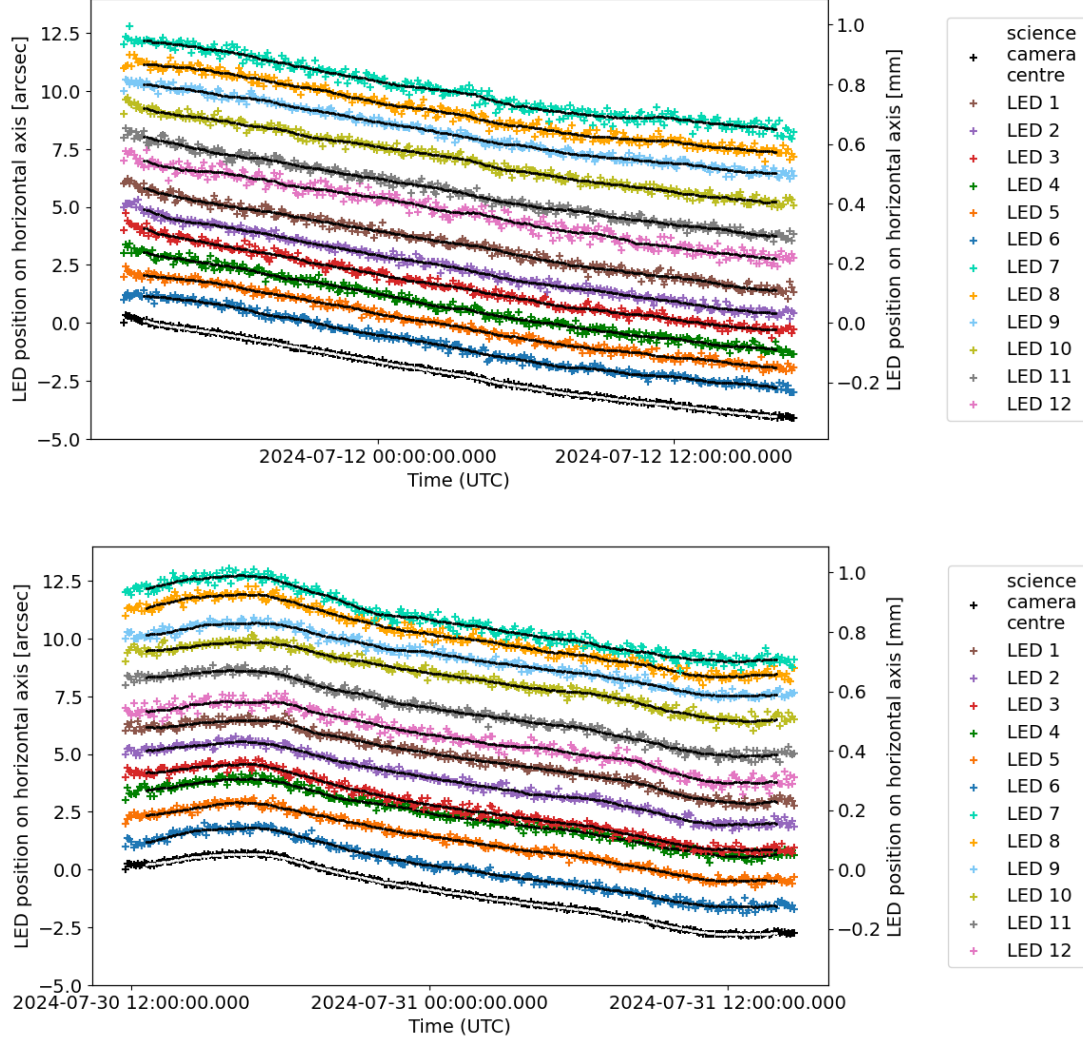


Figure 34: Horizontal positions of the twelve LEDs and of the science camera centre (black data points) for the first campaign (top) and second campaign (bottom) are plotted. The first image of the current campaign is subtracted, then each of the curves is shifted on the y-axis by 1 arcsec relating to the previous one for visualisation. The running averages are plotted as black (white) lines.

position is plotted in Figure 35. During the 10 days the science camera centre position changes by approximately 3.5 arcsec in vertical direction and by approximately 17 arcsec in horizontal direction. Hence, the LEDs did not settle concerning their movement, but followed a constant trend of moving downwards and to the left with some fluctuations. This is expected to improve substantially for the FlashCam set-up planned for CTA due to better set-up conditions concerning material and installation.

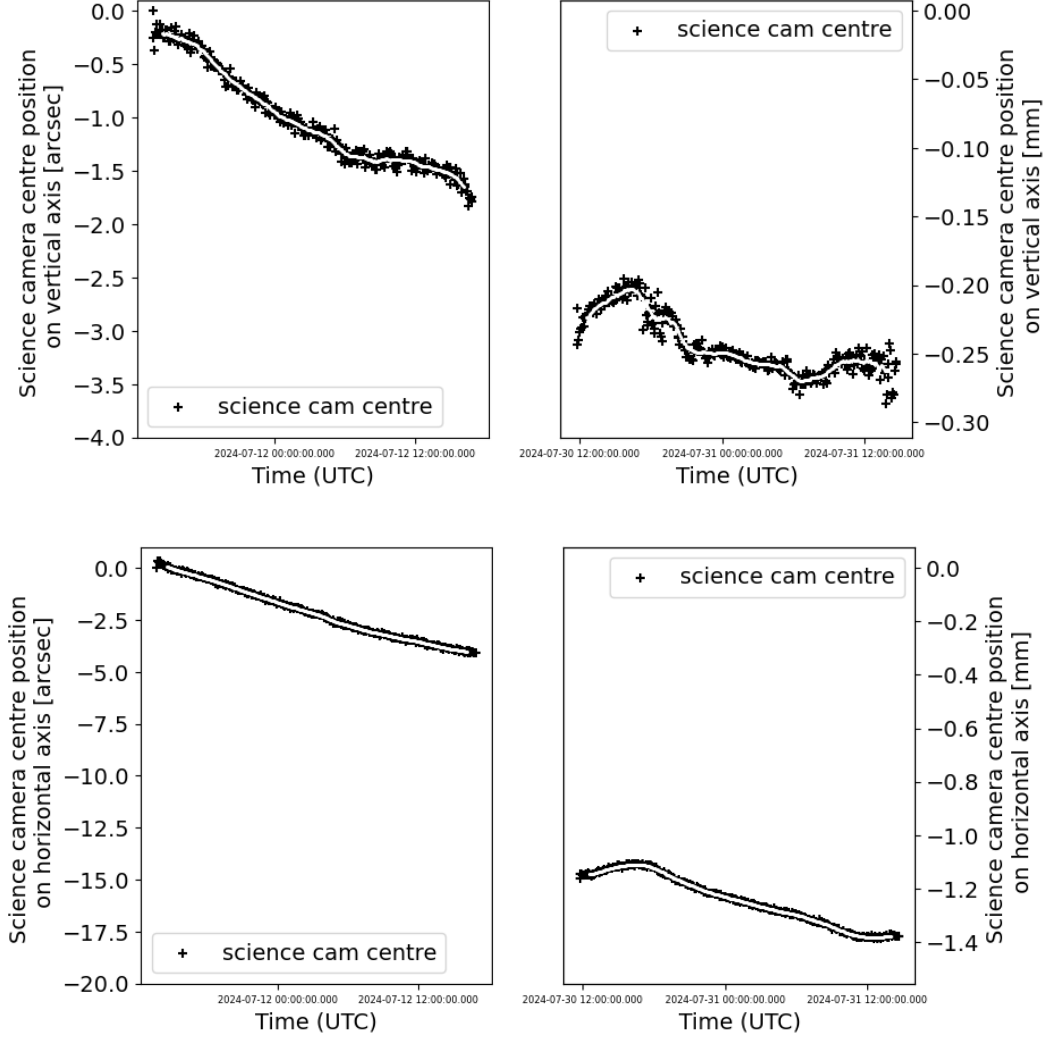


Figure 35: Relative science camera centre positions for the first (left) and second (right) campaign. Top: vertical positions, Bottom: horizontal positions. Starting image of the first campaign subtracted from the images of both campaigns to visualise the full time development. White line: running average.

#### 4.4.2 Deviations of LED positions and pointing precision

In chapter 4.4.1 the minimum LED movement is found to be 1 arcsec from the diagrams in Figure 33 showing that a visual determination of changes in this range is possible. Hence, the contribution of the centre determination to the pointing accuracy must be lower than this value and therefore is well within the 7 arcsec criterion.

Apart from the temporal position deviation of the LEDs, a spacial deviation of their positions from the average can be observed. In order to determine the contribution to the pointing accuracy in the next step, the running average is subtracted from the respective LED positions. These LED position deviations from the average are plotted

as histograms for each of the twelve LEDs as shown in Appendixes A.6 - A.9. The histogram for LED 12 is much broader. This LED is already found in section 4.3 to have lower flux and peak intensity. A potential reason for this anomaly might be an insufficient size or shape of the pinhole in front of this particular LED.

The same procedure is done for the science camera centres and shown in Figure 36 for the vertical deviations and in Figure 37 for the horizontal deviations, exemplarily compared to LED 11. As expected it is directly visible that the distribution for the camera centre deviation, determined from twelve spots, is much narrower than for a single spot.

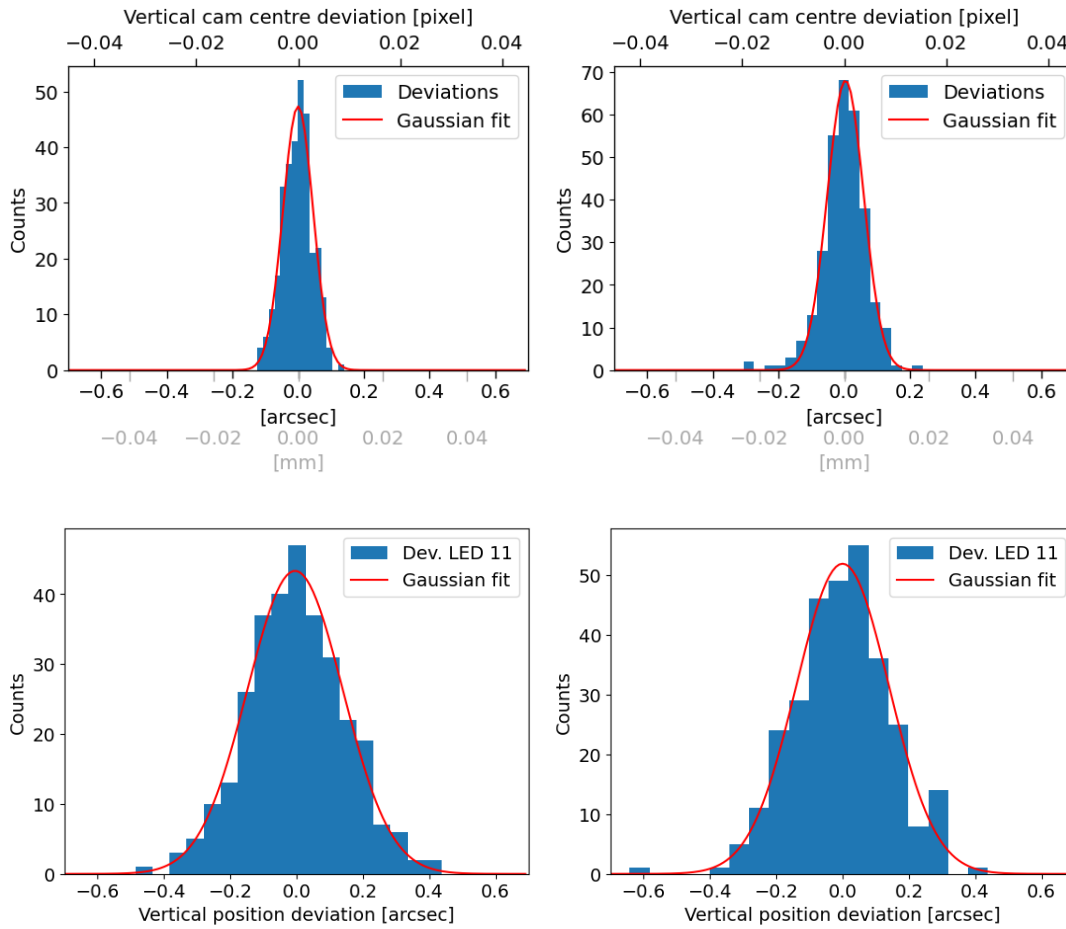


Figure 36: Histograms of the vertical position deviations (from the corresponding running average values) of the science camera centre (top) and an exemplary LED (bottom, LED 11). Left: 1st campaign, right: 2nd campaign. Red: Gaussian fits (see Equation 1). All  $\sigma_{\text{vert}}$  values in Appendix A.10.

A Gaussian (see Equation 1) is fitted to the histograms. The  $\sigma$  values of all Gaussian fits for the twelve LEDs and the science camera centre in vertical and horizontal direction,

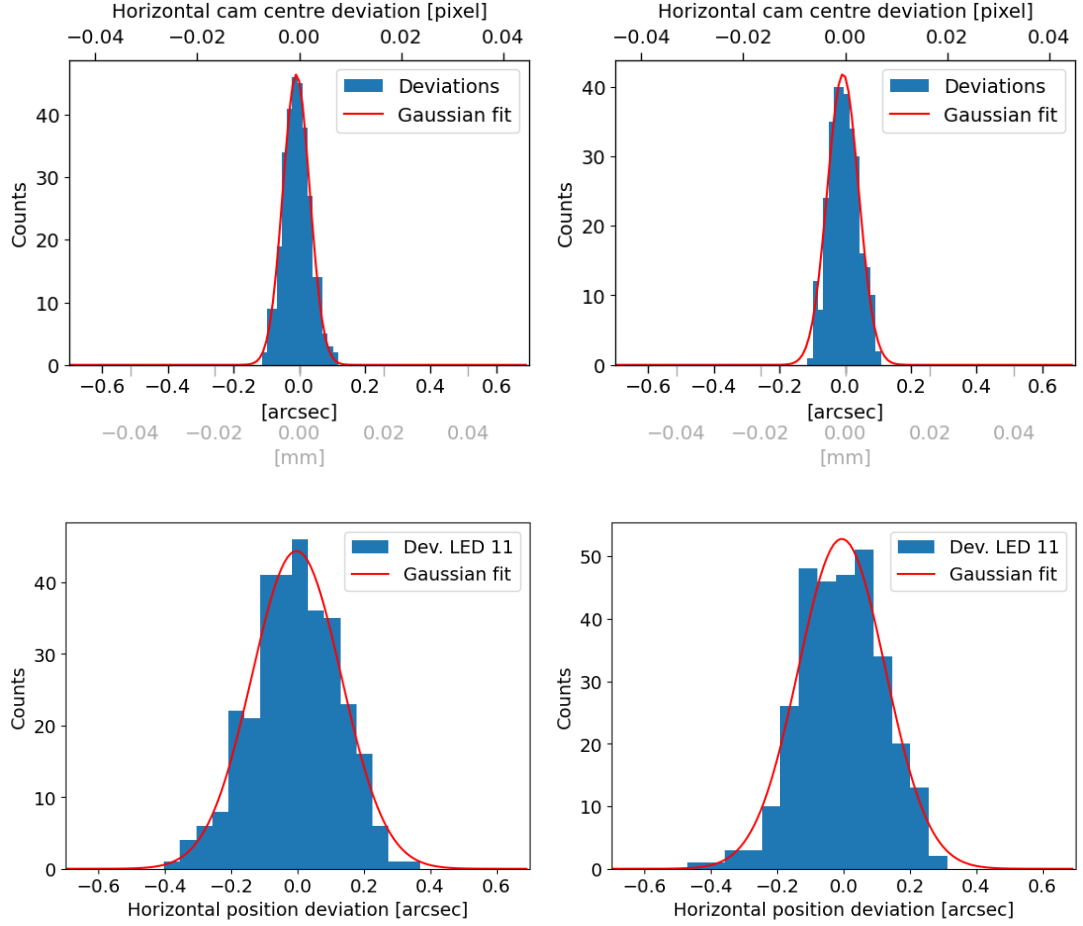


Figure 37: Histograms of the horizontal position deviations (from the corresponding running average values) of the science camera centre (top) and an exemplary LED (bottom, LED 11). Left: 1st campaign, right: 2nd campaign. Red: Gaussian fits (see Equation 1). All  $\sigma_{\text{horiz}}$  values in Appendix A.10.

each, are given in Appendix A.10 for both campaigns. The mean  $\sigma_{\text{LED}}$  values averaged over both campaigns are

$$\bar{\sigma}_{\text{LED,vert}} = (0.146 \pm 0.008) \text{ arcsec} \quad (6)$$

$$\bar{\sigma}_{\text{LED,horiz}} = (0.134 \pm 0.007) \text{ arcsec}. \quad (7)$$

Table 2 contains the four  $\sigma_{\text{centre}}$  and two  $\bar{\sigma}_{\text{centre}}$  values for the vertical and horizontal deviations in both campaigns in pixel, arcsec and mm. The  $\bar{\sigma}_{\text{centre}}$  values corresponds to the pointing precision as it gives a measure of how well the science camera centre



	$10^{-3}[\text{pixel}]$	$10^{-3}[\text{arcsec}]$	$[\mu\text{m}]$
Campaign 1			
$\sigma_{\text{centre,vert}}$	$2.96 \pm 0.18$	$46.0 \pm 2.8$	$3.57 \pm 0.22$
$\sigma_{\text{centre,horiz}}$	$2.63 \pm 0.09$	$40.7 \pm 1.3$	$3.17 \pm 0.11$
Campaign 2			
$\sigma_{\text{centre,vert}}$	$3.58 \pm 0.08$	$55.5 \pm 1.3$	$4.31 \pm 0.11$
$\sigma_{\text{centre,horiz}}$	$3.07 \pm 0.16$	$47.6 \pm 2.5$	$3.70 \pm 0.19$
mean			
$\bar{\sigma}_{\text{centre,vert}}$	$3.27 \pm 0.14$	$50.7 \pm 2.1$	$3.94 \pm 0.16$
$\bar{\sigma}_{\text{centre,horiz}}$	$2.85 \pm 0.13$	$44.1 \pm 2.0$	$3.43 \pm 0.15$

Table 2: Fit parameter  $\sigma$  of the Gaussian fit (see Equation 1) to the histograms of the vertical and horizontal science camera position deviations for both campaigns in Figure 36 and 37.

can be determined by the pointing method. The result is:

$$\bar{\sigma}_{\text{centre,vert}} = (3.27 \pm 0.14) \times 10^{-3} \text{ pixel} \quad (8)$$

$$\hat{=} (50.7 \pm 2.1) \times 10^{-3} \text{ arcsec} \quad (9)$$

$$\hat{=} (3.94 \pm 0.16) \mu\text{m} \quad (10)$$

$$\bar{\sigma}_{\text{centre,horiz}} = (2.85 \pm 0.13) \times 10^{-3} \text{ pixel} \quad (11)$$

$$\hat{=} (44.1 \pm 2.0) \times 10^{-3} \text{ arcsec} \quad (12)$$

$$\hat{=} (3.43 \pm 0.15) \mu\text{m}. \quad (13)$$

The values are slightly larger than the  $\bar{\sigma}_{\text{LED}}$  values weighted by the factor  $\frac{1}{\sqrt{12}}$  given as

$$\bar{\sigma}_{\text{led,vert}} \cdot \frac{1}{\sqrt{12}} = (42.1 \pm 2.3) \times 10^{-3} \text{ arcsec} \quad (14)$$

$$\bar{\sigma}_{\text{led,horiz}} \cdot \frac{1}{\sqrt{12}} = (38.6 \pm 2.1) \times 10^{-3} \text{ arcsec}. \quad (15)$$

Hence, the result for the science camera centre position is more precise than for one single LED by almost the expected factor of  $\sqrt{12} \approx 3.5$  due to the ring fit over the twelve LEDs. Considering the limit of 7 arcsec as total pointing accuracy for all influencing aspects, the values of  $(50.7 \pm 2.1) \times 10^{-3} \text{ arcsec}$  and  $(44.1 \pm 2.0) \times 10^{-3} \text{ arcsec}$  as measure for precision of the ring fit method is quite satisfactory. This is particularly valid taking into account that the position deviations are determined precisely in spite of the flexible material of the mock-up. By a comparison to the intended CTA pointing criterion of 7 arcsec it can be pointed out, that less than 1 % of the maximum pointing accuracy must be reserved for the determination of the pointing direction of the Cherenkov camera, only. Hence, the contribution of the centre determination to the total error budget is negligible.

## 5 Summary and Outlook

A well-operating and precise pointing method is essential for the pointing accuracy of Cherenkov telescopes as their main objective (apart from energy determination) is to identify the source of the observed gamma radiation. The pointing accuracy is affected by several factors such as temperature and rigidity of the set-up. A rather substantial contribution will come from the mirror facets of the telescope dish, e.g. due to misalignment, variations in production and degradation over time. The pointing model is supposed to analyse deviations from the perfect pointing due to these impacts and to facilitate corrections to support precise direction reconstruction. To this end, the pointing model itself must be carefully tested to provide sufficient reliability and accuracy.

The chosen method to determine the Cherenkov camera centre for the Medium-Sized Telescopes of CTA is based on a ring fit through twelve LEDs. These were mounted in circular shape around the centre of the Cherenkov camera. The pointing camera took images of this set-up which were provided to the CTA pointing software for spot extraction and ring fit analysis. The concept is supposed to fulfil the total CTA pointing accuracy criterion of 7 arcsec. In this thesis, the contribution of the Cherenkov camera centre determination to the total error budget was analysed.

The pointing method features a single CCD concept with a simultaneous imaging of stars and LEDs. In order to verify the optical conditions, a set-up was created containing an LED behind a pinhole as suitable light source for the pointing set-up. The stability of the test set-up regarding temperature and focal accuracy was tested and found to be sufficient.

The pointing set-up has to provide a well controlled brightness of the LED spots to enable simultaneous imaging of the LEDs and the stars. Two demands are made on the imaged spots:

- The spots have to cover a sufficient number of pixels to enable a reliable position reconstruction. A slight defocusing was already given by adjusting the hyperfocal distance. The spot widths are correlated to the pinhole sizes. The final setting achieved spot widths of about 4 – 5 pixels which can be assumed as sufficient.
- The intensity of the spots must be similar to the one of the stars. It can be adjusted by the current control to a certain extent, but had to be reduced by factor  $10^3$  by use of a filter to reach the desired range. A diffuser was chosen to support an isotropic illumination, especially as the LEDs have positions lying off the optical axis.

A 3D printed assembly consisting of LED holder, two holders for filters or diffuser and a pinhole was used to test the attenuation effects of several combinations of filters and diffuser. The combination of a neutral density filter with nominal optical density 1 and a diffuser attenuating the LED light by factor 100 between LED and pinhole was determined suitable for the desired illumination. It was taken into account that the exposure time of night sky campaigns has not been fixed yet for operation. In

the supposed exposure time range of 5 s – 20 s and the available LED current range of 0 mA – 20 mA, both parameters were modified and adjusted to each other. The setting of 10 s exposure time and 10 mA current per LED was found as optimum solution for further measurements. Moreover, this combination still allows a wide control range via the LED current for fine tuning.

A critical parameter that was identified is the size and quality of the pinhole illuminated by the LED. The simple 3D printed pinholes employed in a first set-up were found to vary too much in size and quality. They were improved to a suitable level by melting them up with a hot wire in a post-processing step.

Next, a mock-up of the Cherenkov camera front was constructed and twelve of the previously tested LED light sources are mounted in a circle on their predefined positions to determine the contribution of the pointing set-up configuration to the total CTA pointing accuracy. The prepared choice of filter, diffuser, pinhole size, exposure time, LED current and a customised filter holder assembly was applied. This special combination delivered the desired spot sizes and intensities for the lab simulation of the nominal LED arrangement and thereby offered the possibility of further vernier adjustment by the current control.

The stability of this set-up regarding background, camera temperature and focal length was verified by acquiring data in two series of 325 images within 27 h each, separated by 10 days. All parameters were found to be virtually constant. The LED intensity initially decreased, but settled between the series.

The main result was the verification of the pointing accuracy. Even with effects of temperature and optical stability being negligible, it was found that the observed LED positions change over time due to the flexible and wobbly properties of the used mock-up. The precision of the method was determined by analysing the position residuals with respect to a running average of the reconstructed positions. The science camera centre was determined by a ring fit through the LEDs following the standard implementation of a maximum likelihood fit. Each LED spot could be determined with few arcsecs precision, already fulfilling the 7 arcsec criterion. For the science camera centre the precision achieved is

$$\begin{aligned}\bar{\sigma}_{\text{cent,vert}} &= (50.7 \pm 2.1) \times 10^{-3} \text{ arcsec} \\ \bar{\sigma}_{\text{cent,horiz}} &= (44.1 \pm 2.0) \times 10^{-3} \text{ arcsec}.\end{aligned}$$

This is close to the expected improvement of factor  $\sqrt{12} \approx 3.5$  compared to a single LED system and is more than two orders of magnitude smaller than the total pointing accuracy requirement. Hence, the determination of the pointing direction of the Cherenkov camera centre contributes by less than 1 % of this criterion to the pointing accuracy and therefore can be assumed negligible. This highlights the suitability of the pointing method for use in the Medium-Sized Telescopes of CTA.

For the application in the Atacama desert the mounting of the LEDs to the Cherenkov camera front will technically improve, and material of higher stability will be used.

From the experiments done in terms of this thesis, the most critical parameters for the final design can be deduced. These are mainly the size and quality of the pinholes and a suitable choice of diffuser and neutral density filters. The filter- and LED holder could be replaced by a water- and dust tight solution, protecting it from environmental impacts. The size of the hole transmitting the LED light will be a relevant factor for the adjustment of the intensity. As a result of the PCAM image analysis with the used mock-up, it can be stated, that the Cherenkov camera centre determination contributes by 1 % to the desired CTA pointing criterion of 7 arcsec, only. Therefore, the contribution of this method to the total error budget is negligible. The described determination of the Cherenkov camera centre can be assumed as suitable for application at the MSTs of CTA.



## Acronyms

**CTA** Cherenkov Telescope Array. 2, 3, 4, 6, 13, 19, 34, 38, 39, 40, 41

**H.E.S.S.** High Energy Stereoscopic System. 2

**IACTs** Imaging Air Cherenkov Telescopes. 2, 3

**MAGIC** Major Atmospheric Gamma-ray Imaging Cherenkov telescopes. 2

**MST** Medium-Sized Telescope. 4, 6, 9, 10, 13, 22

**MSTs** Medium-Sized Telescopes. 2, 3, 4, 6, 41

**PCAM** Pointing Camera. 5, 6, 7, 8, 9, 10, 11, 12, 24, 27, 30, 31, 32, 41

**VERITAS** Very Energetic Radiation Imaging Telescope Array System. 2



## A Appendix

### A.1 Fit parameters for plot "peak intensity over current"

exp.time	a	$p_0$
$10^{-2}$ s	$4850 \pm 70$	$-5000 \pm 600$
$10^{-3}$ s	$538 \pm 6$	$-630 \pm 70$
$10^{-4}$ s	$80.3 \pm 2.5$	$-90 \pm 30$

Table 3: Fit parameters of the linear fits (equation: see section 3.3.1) to the plots "peak intensity over current" in Figure 12.



## A.2 LED spot position in y axis over peak intensity

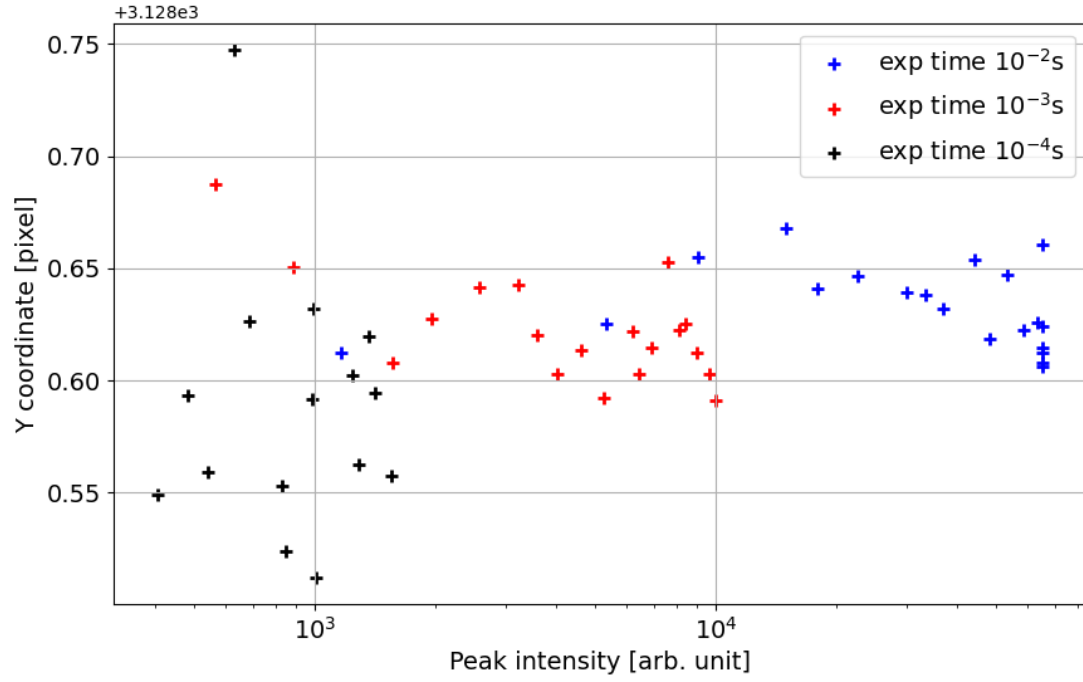


Figure 38: Y coordinate of the extracted LED spot positions as a function of the peak intensity. For the x coordinate see Figure 13.

### A.3 Fit parameters of Gaussian fit to x/y projections for exemplary LED spot

	A	$x_0$	$\sigma$
proj. on y axis	$110000 \pm 3000$	$9.324 \pm 0.028$	$0.894 \pm 0.029$
proj. on x axis	$110400 \pm 2600$	$10.080 \pm 0.025$	$0.900 \pm 0.024$

Table 4: Fit parameters of the Gaussian fit (Equation 1) to the projection on the x/y axis in Figure 18.

#### A.4 Fit parameters of Gaussian fit to x/y projections for LED spot with OD 1 filter and diffuser

	A	$x_0$	$\sigma$
proj. on y axis	$90900 \pm 1900$	$9.128 \pm 0.022$	$0.865 \pm 0.021$
proj. on x axis	$90300 \pm 1900$	$9.853 \pm 0.022$	$0.872 \pm 0.021$

Table 5: Fit parameters of the Gaussian fit (Equation 1) to the projection on the x/y axis in Figure 20.

## A.5 Hole sizes in the final set-up

hole diameter [mm]		Peak Intensity [arb.unit]
0.52145	A	(40732)
0.52669	B	46626
0.50825	C	47125
0.52980	D	48082
0.54261	E	49661
0.51893	F	51807
0.53019	G	51835
0.51582	H	52740
0.52203	I	53986
0.50709	J	54131
0.51349	K	54706
0.51602	L	58082
0.51660	M	58831
0.51388	N	(58954)
0.50961	O	(59218)
0.50340	P	(59345)
0.52184	Q	(59664)
0.51738	R	(59831)
0.52572	S	(61800)

Table 6: Left: diameters of 19 holes melted by a 0.5 mm hot wire, measured under a microscope. Right: Peak intensities of those 19 pinholes. The ones in parentheses are not taken for the set-up. See section 4.2.

## A.6 Histograms of vertical LED position deviations for the first campaign

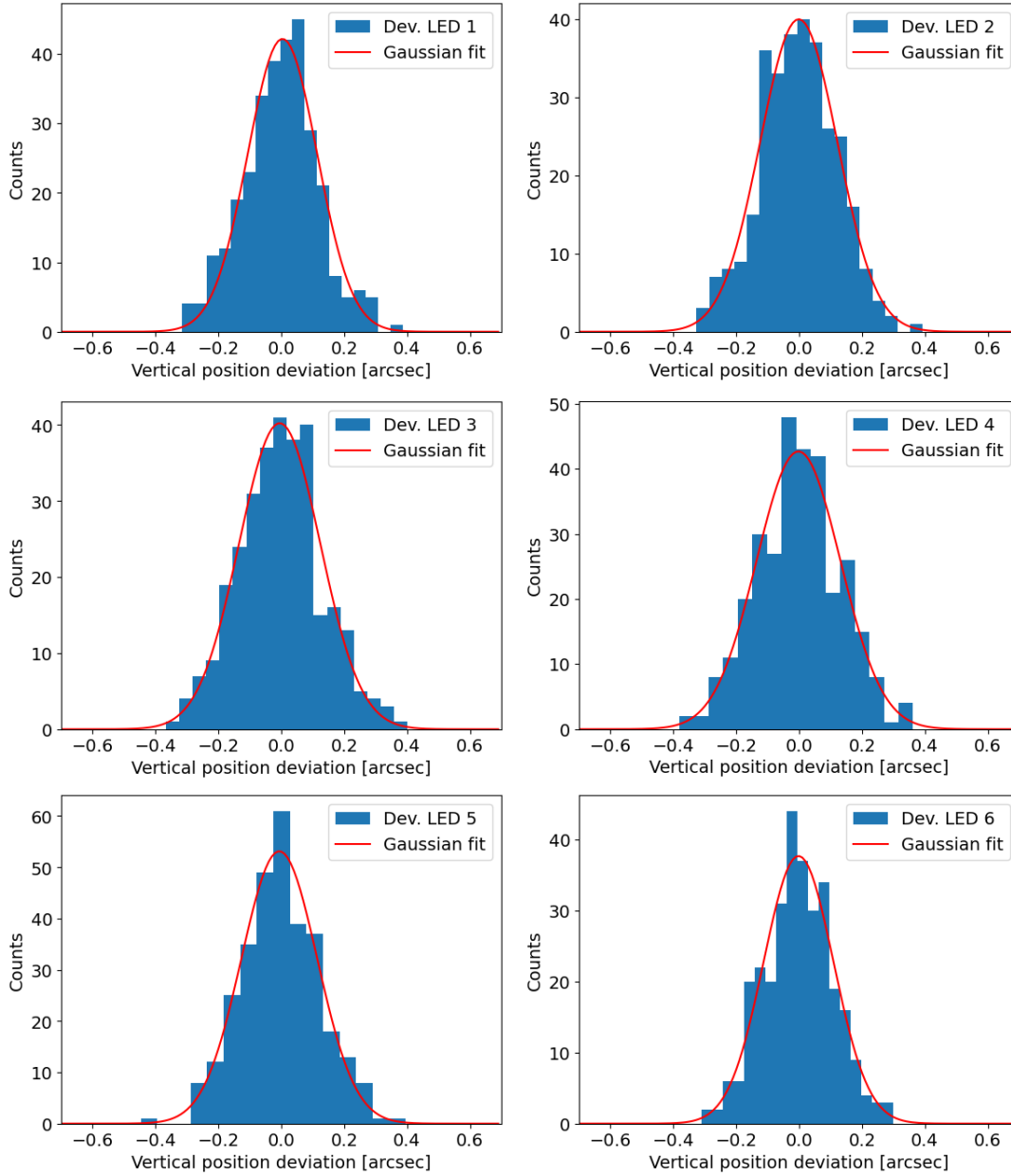


Figure 39: Histograms of LED position deviations on vertical axis for LED 1-6, first campaign. See section 4.4.2.

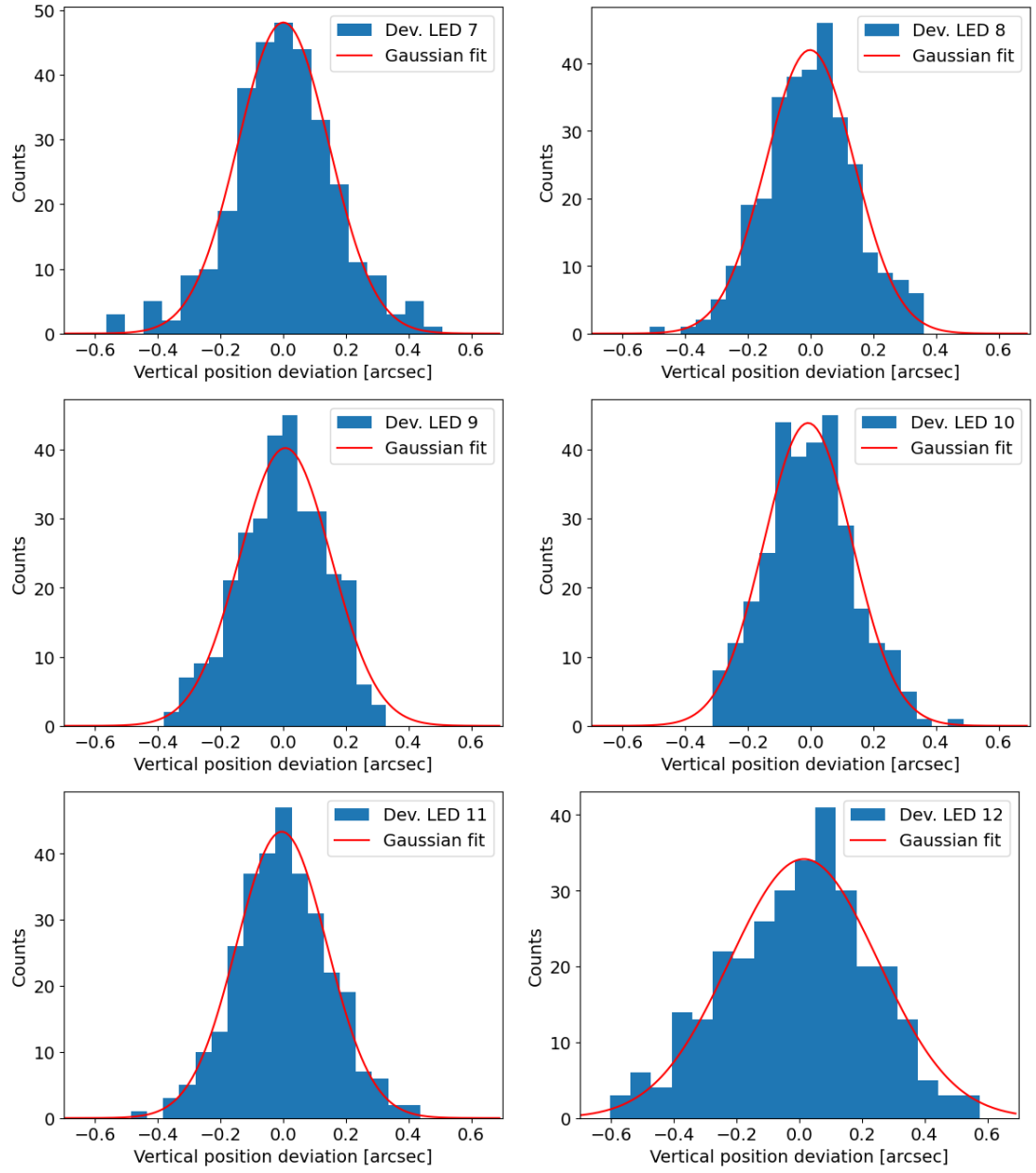


Figure 40: Histograms of LED position deviations on vertical axis for LED 7-12, first campaign. See section 4.4.2.

## A.7 Histograms of horizontal LED position deviations for the first campaign

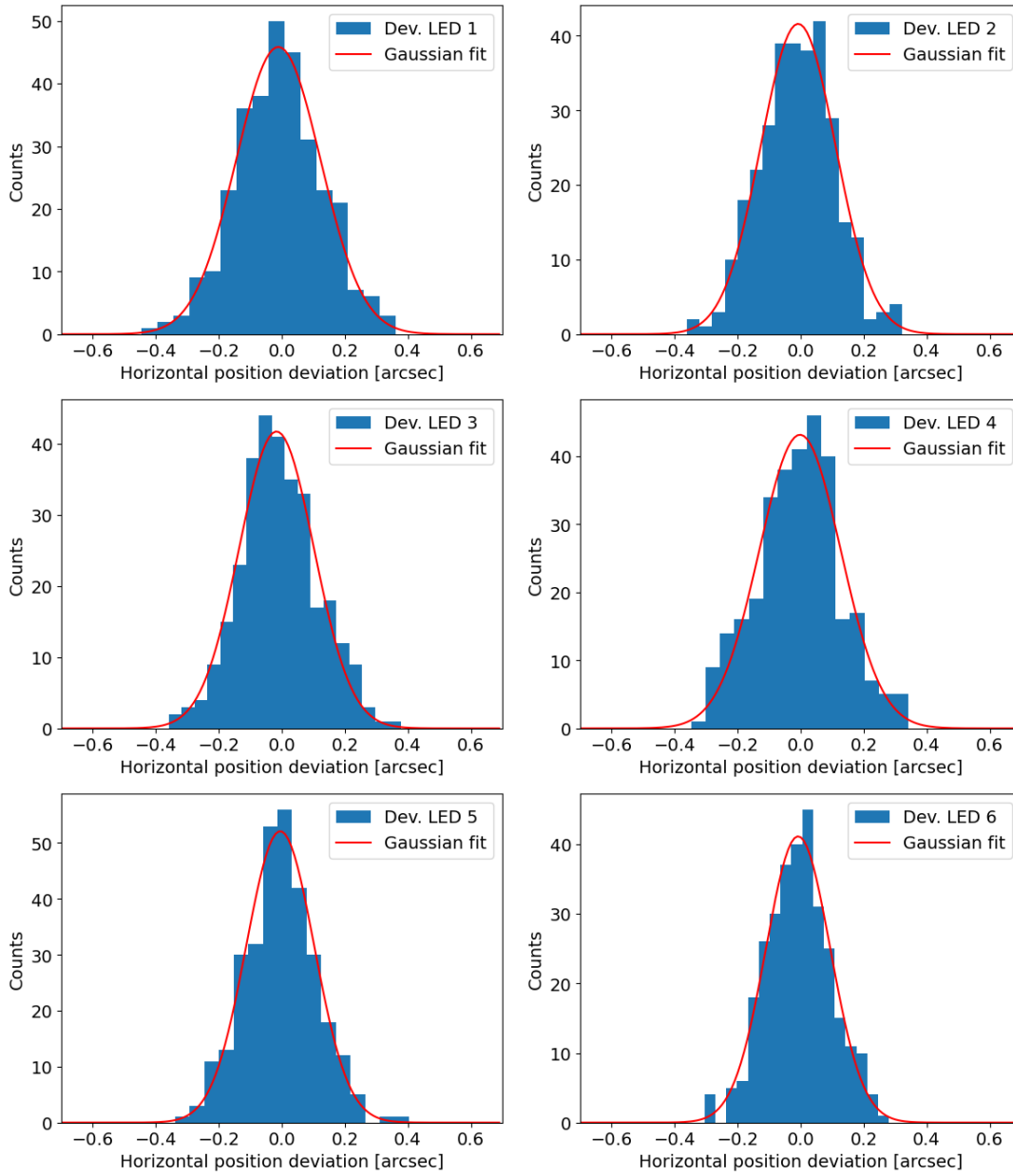


Figure 41: Histograms of LED position deviations on horizontal axis for LED 1-6, first campaign. See section 4.4.2.

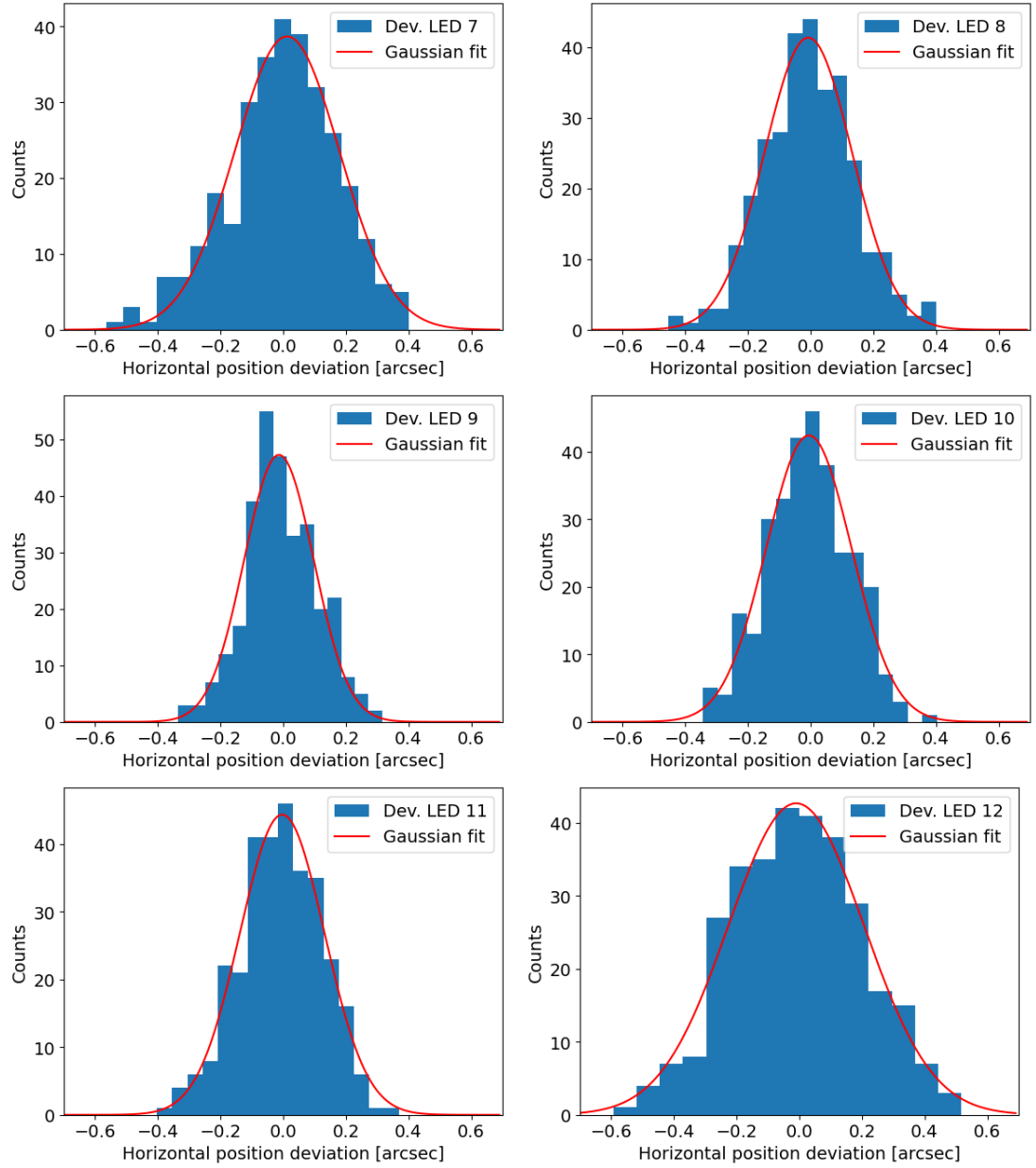


Figure 42: Histograms of LED position deviations on horizontal axis for LED 7-12, first campaign. See section 4.4.2.



## A.8 Histograms of vertical LED position deviations for the second campaign

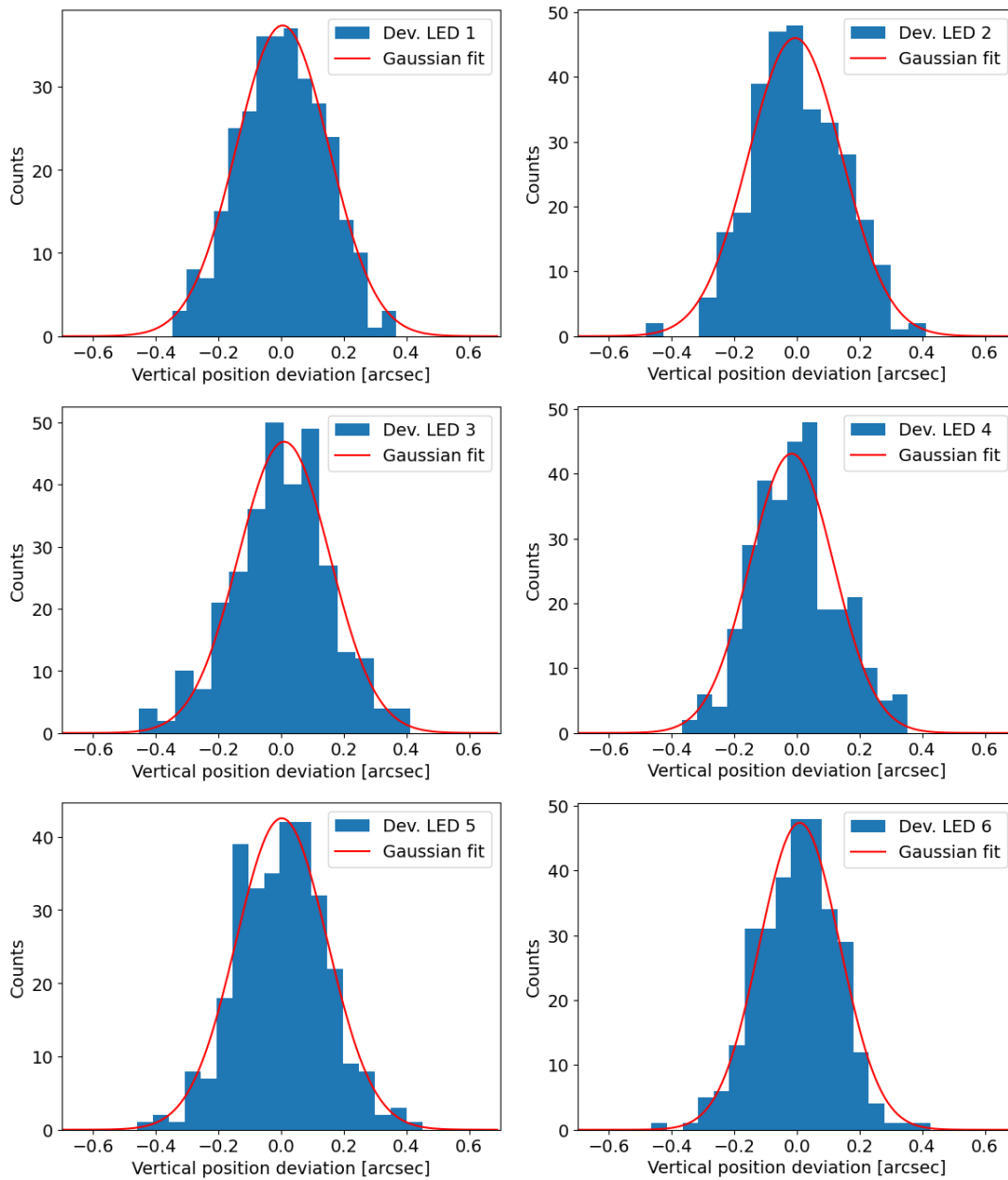


Figure 43: Histograms of LED position deviations on vertical axis for LED 1-6, second campaign. See section 4.4.2.

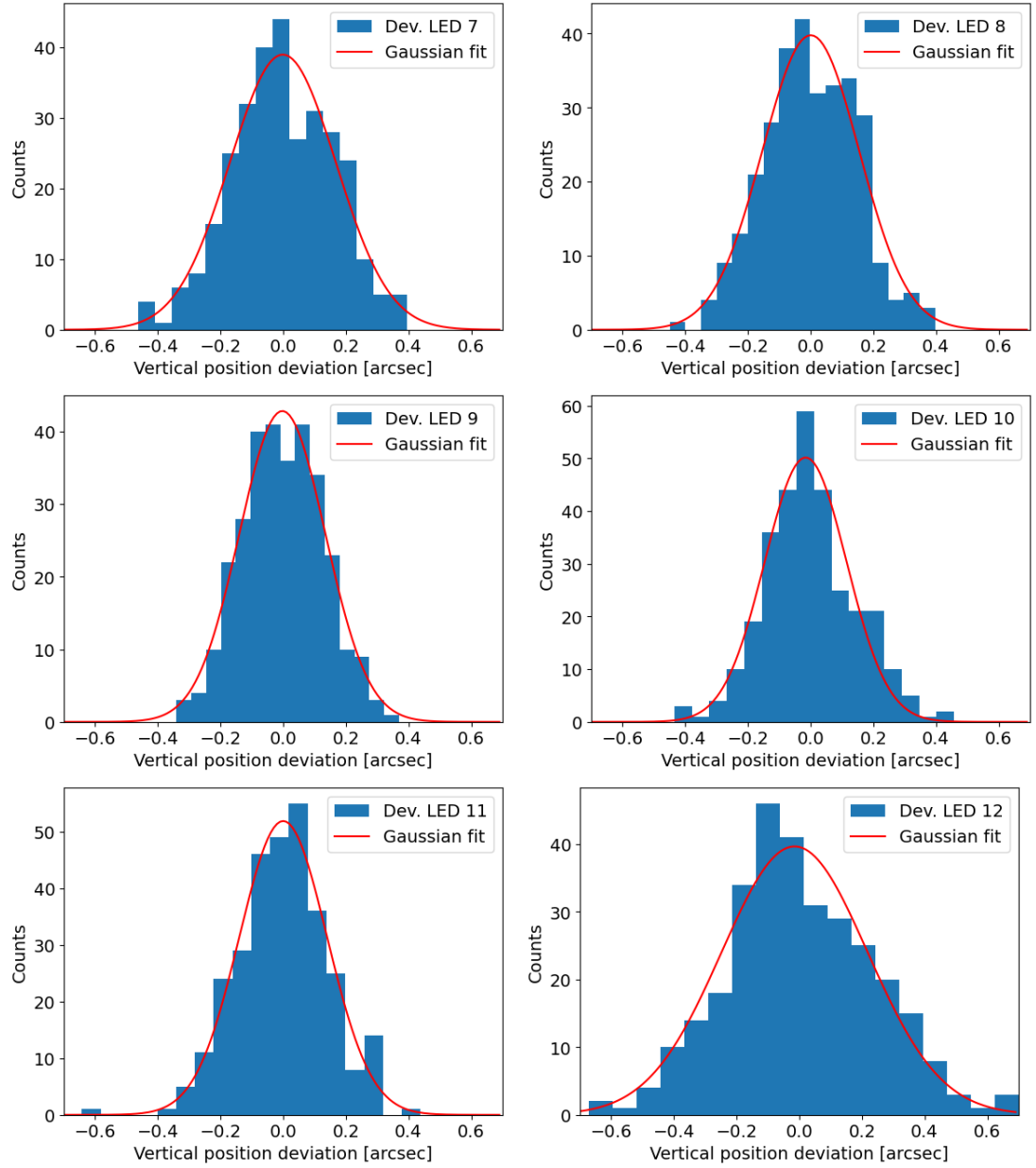


Figure 44: Histograms of LED position deviations on vertical axis for LED 7-12, second campaign. See section 4.4.2.

## A.9 Histograms of horizontal LED position deviations for the second campaign

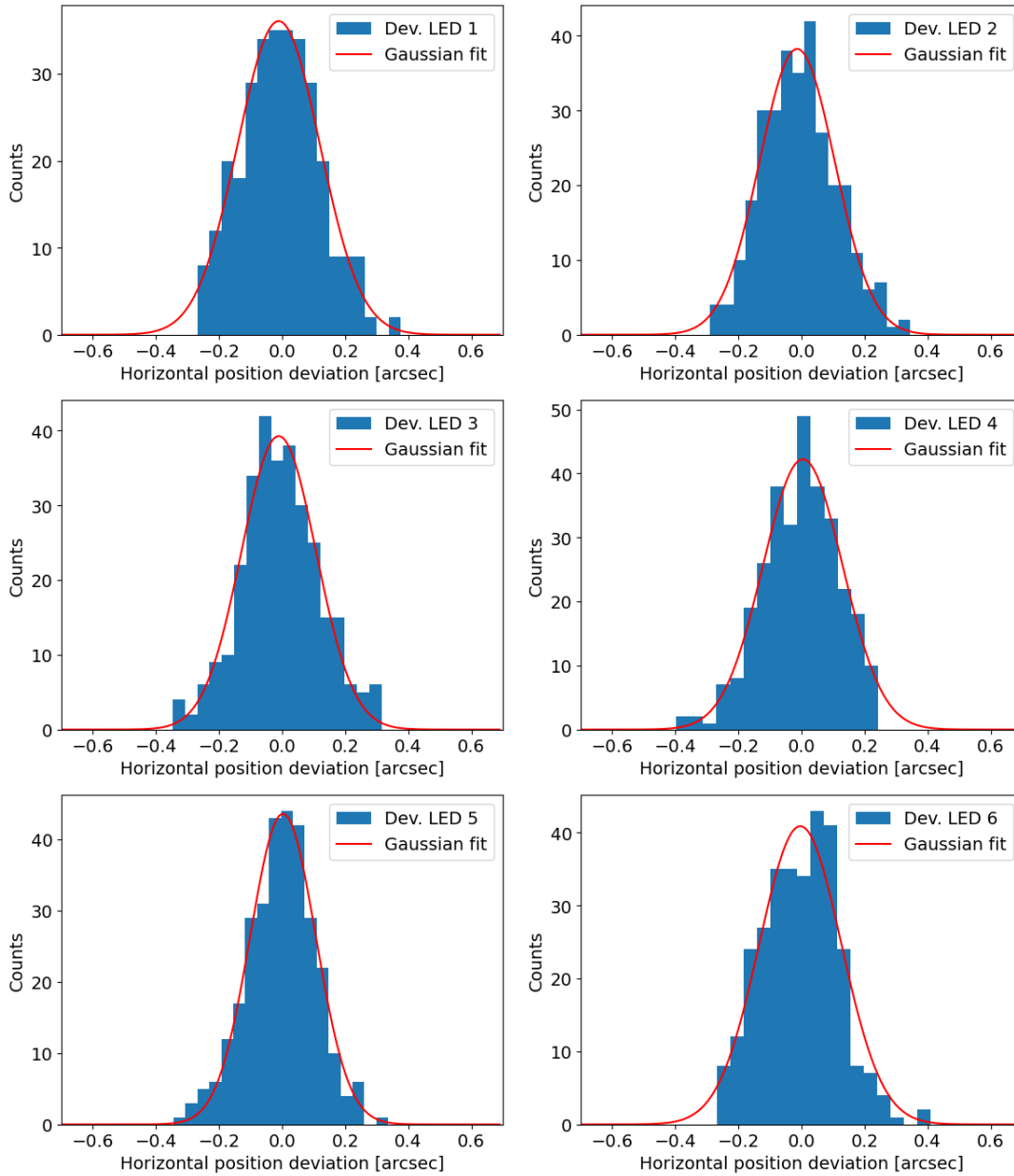


Figure 45: Histograms of LED position deviations on horizontal axis for LED 1-6, second campaign. See section 4.4.2.

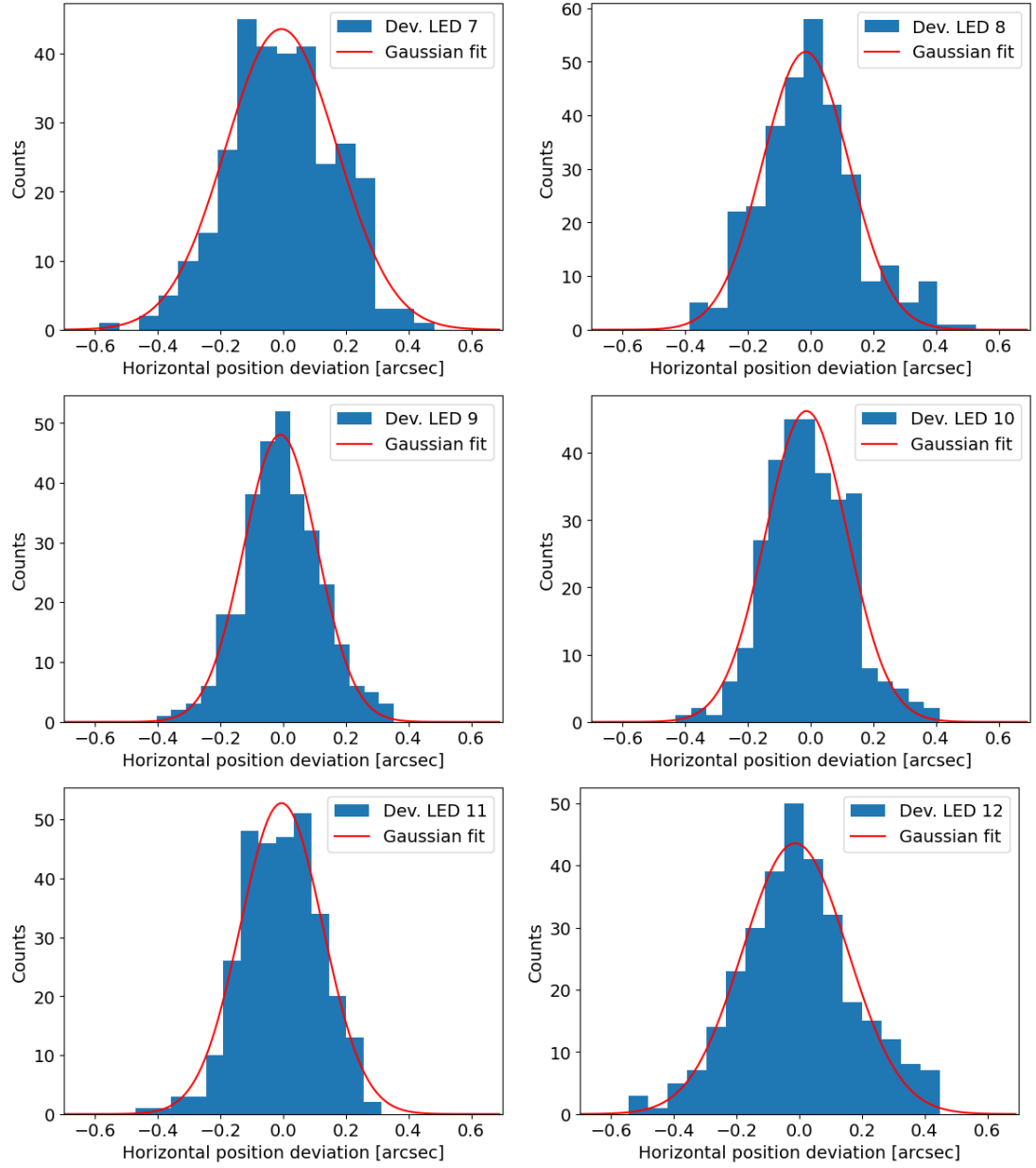


Figure 46: Histograms of LED position deviations on horizontal axis for LED 7-12, second campaign. See section 4.4.2.

### A.10 Fit parameter $\sigma$ of Gaussian fit to vertical/horizontal position deviations for both campaigns

	$\sigma_{\text{vert}}$ [arcsec]	$\sigma_{\text{horiz}}$ [arcsec]
LED 1	$0.111 \pm 0.006$	$0.135 \pm 0.006$
LED 2	$0.123 \pm 0.006$	$0.120 \pm 0.009$
LED 3	$0.129 \pm 0.007$	$0.119 \pm 0.006$
LED 4	$0.134 \pm 0.009$	$0.131 \pm 0.009$
LED 5	$0.120 \pm 0.006$	$0.108 \pm 0.005$
LED 6	$0.111 \pm 0.007$	$0.104 \pm 0.007$
LED 7	$0.146 \pm 0.005$	$0.168 \pm 0.008$
LED 8	$0.141 \pm 0.006$	$0.140 \pm 0.006$
LED 9	$0.146 \pm 0.008$	$0.111 \pm 0.009$
LED 10	$0.141 \pm 0.007$	$0.136 \pm 0.007$
LED 11	$0.144 \pm 0.005$	$0.137 \pm 0.006$
LED 12	$0.237 \pm 0.014$	$0.219 \pm 0.019$
mean	$0.140 \pm 0.007$	$0.135 \pm 0.007$
$\frac{1}{\sqrt{12}}$ mean	$0.0405 \pm 0.0021$	$0.0389 \pm 0.0020$
centre	$0.0460 \pm 0.0028$	$0.0407 \pm 0.0013$

Table 7: Fit parameter  $\sigma$  of the Gaussian fit (Equation 1) to the histograms in Figure 36 and 37 and section A.6 and A.7 (first campaign, histograms of vertical and horizontal position deviations).

	$\sigma_{\text{vert}}$ [arcsec]	$\sigma_{\text{horiz}}$ [arcsec]
LED 1	$0.148 \pm 0.005$	$0.130 \pm 0.009$
LED 2	$0.149 \pm 0.008$	$0.117 \pm 0.008$
LED 3	$0.146 \pm 0.010$	$0.118 \pm 0.006$
LED 4	$0.134 \pm 0.012$	$0.126 \pm 0.007$
LED 5	$0.146 \pm 0.009$	$0.104 \pm 0.004$
LED 6	$0.128 \pm 0.006$	$0.129 \pm 0.012$
LED 7	$0.170 \pm 0.011$	$0.174 \pm 0.012$
LED 8	$0.155 \pm 0.009$	$0.137 \pm 0.009$
LED 9	$0.137 \pm 0.006$	$0.118 \pm 0.007$
LED 10	$0.131 \pm 0.009$	$0.131 \pm 0.008$
LED 11	$0.140 \pm 0.007$	$0.130 \pm 0.010$
LED 12	$0.233 \pm 0.014$	$0.167 \pm 0.009$
mean	$0.151 \pm 0.009$	$0.133 \pm 0.007$
$\frac{1}{\sqrt{12}}$ mean	$0.0437 \pm 0.0026$	$0.0383 \pm 0.0022$
centre	$0.0555 \pm 0.0013$	$0.0476 \pm 0.0025$

Table 8: Fit parameter  $\sigma$  of the Gaussian fit (Equation 1) to the histograms in Figure 36 and 37 and section A.8 and A.9 (second campaign, histograms of vertical and horizontal position deviations).



## Bibliography

- CTA Consortium, J.-F. Glicenstein for the (2010). „The Cherenkov telescope array, an advanced facility for ground based gamma-ray astronomy“. In: *Nuclear Instruments and Methods in Physics Research A*, pp. 46–49.
- CTA-website (2024a). *CTAO-South*. <https://www.ctao.org/emission-to-discovery/array-sites/ctao-south/>. [Online; accessed 20-June-2024].
- (2024b). *Medium-Sized Telescope*. <https://www.ctao.org/emission-to-discovery/telescopes/mst/>. [Online; accessed 12-June-2024].
- (2024c). *The CTAO’s Study Themes*. <https://www.ctao.org/emission-to-discovery/science/study-themes/>. [Online; accessed 12-June-2024].
- (2024d). *The Next Generation High-Energy Discovery Machines*. <https://www.ctao.org/emission-to-discovery/telescopes/>. [Online; accessed 19-June-2024].
- (2024e). *The Origin of Gamma Rays*. <https://www.ctao.org/emission-to-discovery/science/>. [Online; accessed 19-June-2024].
- (2024f). *Turning Light Into Discoveries*. <https://www.ctao.org/emission-to-discovery/science/how-ctao-works/>. [Online; accessed 19-June-2024].
- Eldik, Christopher van (2024). personal correspondence.
- G. Pühlhofer C. Bauer, S. Bernhard M. Capasso S. Diebold F. Eisenkolb D. Florin C. Föhr S. Funk A. Gadola F. Garrecht G. Hermann I. Jung O. Kalekin C. Kalkuhl J. Kasperek T. Kihm R. Lahmann A. Manalaysay A. Marszalek M. Pfeifer P.J. Rajda O. Reimer A. Santangelo T. Schanz T. Schwab S. Steiner U. Straumann C. Tenzer A. Vollhardt Q. Weitzel F. Werner D. Wolf K. Zietara for the CTA Consortium (2015). „FlashCam: a fully-digital camera for the medium-sized telescopes of the Cherenkov Telescope Array“. In: *arXiv:1509.02434v1 [astro-ph.IM]*.
- Garczarczyk, Markus (2022a). „Design and Implementation of the MST Structure Software“. In: Version 1.0, 2022-07-06, MST-STR-TDR-36121000-00012.
- (2022b). „Medium-Sized Telescope Structure Technical Design Report“. In: Version 2.0, 2022-07-07, MST-STR-TDR-36121000-00001.
- Herpich, Jakob (2010). „Testing a Single-CCD-Concept for the H. E. S. S. II Pointing“. MA thesis. University of Heidelberg.
- Lahmann, PD Dr. Robert (2022). „Introduction to Astroparticle Physics“. In: WS 2021/22.
- Naurois, Daniel Mazin Mathieu de (Nov. 2, 2015). „Ground-based detectors in very-high-energy gamma-ray astronomy“. In: *arXiv:1511.00463v1 [astro-ph.IM]*. URL: <https://arxiv.org/pdf/1511.00463> (visited on 2024).
- U. Schwanke T. Murach, P. Wagner G. Spengler for the CTA MST Project, I. Oya D. Melkumyan, and Berlin Germany; DESY Zeuthen Germany; CTA Heidelberg Germany T. Schmidt Humboldt-University (2022). *Control, readout and monitoring for the medium-sized telescopes in the cherenkov telescope array*. <https://accelconf>.

[web.cern.ch/icalepcs2021/papers/mobr02.pdf](http://web.cern.ch/icalepcs2021/papers/mobr02.pdf), doi:10.18429/JACoW-ICALEPCS2021-MOBR02, JACoW Publishing. [Online; accessed 12-June-2024].

Zwoastro (2021). *ZWO ASI2600 Manual*. [https://i.zwoastro.com/zwo-website/manuals/ZWO\\_ASI2600\\_Manual\\_EN.pdf](https://i.zwoastro.com/zwo-website/manuals/ZWO_ASI2600_Manual_EN.pdf). [Online; accessed 07-July-2024].





## Acknowledgements

The successful finish of this bachelor thesis is thanks to a number of people who supported me, some of them for an incredibly long time. In particular, I would like to express my gratitude to

- **Prof. Dr. Christopher van Eldik** for the well-fitting topic, uncomplicated supervision and extensive support. Thanks, that we do science for fun and without stress.
- **Dr. Johannes Schäfer** for numerous answers and explanations, a creative teamwork and constructive supervision of my bachelor thesis. Your desk is a place full of remarkable ideas.
- **My husband** for his incredible patience and profound physics on the sofa around-the-clock.

## Eigenständigkeitserklärung

Hiermit versichere ich, Christina Matzke (21671013), die vorgelegte Arbeit selbstständig und ohne unzulässige Hilfe Dritter sowie ohne die Hinzuziehung nicht offengelegter und insbesondere nicht zugelassener Hilfsmittel angefertigt zu haben. Die Arbeit hat in gleicher oder ähnlicher Form noch keiner anderen Prüfungsbehörde vorgelegen und wurde auch von keiner anderen Prüfungsbehörde bereits als Teil einer Prüfung angenommen.

Die Stellen der Arbeit, die anderen Quellen im Wortlaut oder dem Sinn nach entnommen wurden, sind durch Angaben der Herkunft kenntlich gemacht. Dies gilt auch für Zeichnungen, Skizzen, bildliche Darstellungen sowie für Quellen aus dem Internet.

Mir ist insbesondere bewusst, dass die Nutzung künstlicher Intelligenz verboten ist, sofern diese nicht ausdrücklich als Hilfsmittel von dem Prüfungsleiter bzw. der Prüfungsleiterin zugelassen wurde. Dies gilt insbesondere für Chatbots (insbesondere ChatGPT) bzw. allgemein solche Programme, die anstelle meiner Person die Aufgabenstellung der Prüfung bzw. Teile derselben bearbeiten könnten.

---

Ort, Datum

---

Unterschrift